Table 1
Fifty-percent cell growth inhibitory concentration (IC_{50}) of DACHPt/m and oxaliplatin against human scirrhous gastric cancer OCUM-2-MLN cells.

Drug	IC_{50} (μM)	
	48 h	72 h
DACHPt/m	20.0	12.5
Oxaliplatin	12.5	6.25

exchange of DACHPt from the carboxylic groups of p(Glu) to the chloride ions in the media [28]. The 50% cell growth inhibitory concentration (IC_{50}) of DACHPt/m was approximately 2-fold higher than that of oxaliplatin (Table 1).

3.2. Antitumor activity against bioluminescent orthotopic gastric tumors

OCUM-2MLN cells stably expressing luciferase gene (OCUM-2MLN-Luc) were prepared by the lentiviral transfection. The bioluminescent signal of OCUM-2MLN-Luc after the addition of luciferin was measured by IVIS (Supplementary Fig. S2). As the light glowing from the cells increased linearly with cell density (Supplementary Fig. S2), we can use the light intensity of OCUM-2MLN-Luc to quantify the tumor burden.

The antitumor activity of oxaliplatin and DACHPt/m was studied in mice bearing orthotopic OCUM-2MLN-Luc tumors that have

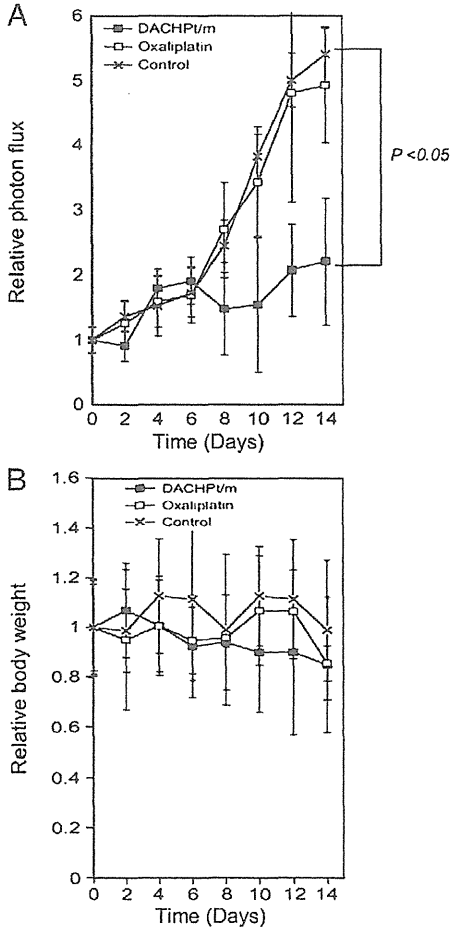

Fig. 2. Antitumor activity of oxaliplatin and DACHPt/m against bioluminescent OCUM-2-MLN-Luc orthotopic gastric cancer. A, Relative photon flux from the tumors after the injection of saline, oxaliplatin 8 mg/kg and DACHPt/m 4 mg/kg on days 0, 2 and 4. B, Relative body weight of the mice. Data are expressed as a mean ± SE ($n = 5$).

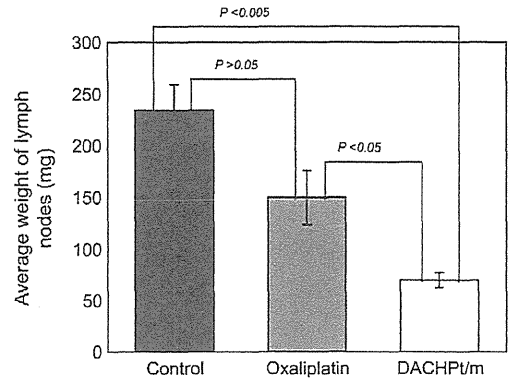

Fig. 3. Weight of the metastatic lymph nodes at the end of the antitumor activity experiment (day 14). Data are expressed as a mean ± SE ($n = 5$).

already developed metastasis to the lymph nodes. The mice were treated intravenously 3 times at 0, 2 and 4 days with oxaliplatin at 8 mg/kg or DACHPt/m at 4 mg/kg on a Pt basis. The photon flux (photons per second) from the bioluminescent tumors was assessed by IVIS every second day. Consequently, oxaliplatin failed to show any antitumor effect against the OCUM-2MLN-Luc tumors as the photon flux of oxaliplatin-treated mice was comparable to that of untreated mice (Fig. 2A). In contrast, the mice treated with DACHPt/m showed significantly lower relative photon flux compared with untreated and oxaliplatin-treated mice (Fig. 2A) without significant body weight loss (Fig. 2B), indicating a significant antitumor activity against the orthotopic gastric tumors.

3.3. Growth inhibition of lymph node metastasis

At the end of the antitumor activity study, the mice were sacrificed and the metastatic lymph nodes were collected and weighed. As shown in Fig. 3, the weights of the lymph nodes in DACHPt/m-treated mice were approximately four and two times lower than those in untreated mice and oxaliplatin-treated mice, respectively, suggesting that DACHPt/m might effectively inhibit the growth of the metastatic lymph nodes and their efficacy might surpass that of oxaliplatin.

3.4. Biodistribution of DACHPt/m in orthotopic gastric tumors and metastatic lymph nodes

DACHPt/m gradually accumulated in the orthotopic tumors due to the EPR effect, achieving approximately 10% of injected dose per gram of tumor tissue at 24 h (Fig. 4A). The tumor accumulation at 24 h for DACHPt/m was 6 times higher than oxaliplatin (Fig. 4A). DACHPt/m also showed enhanced accumulation in sentinel and distant metastatic lymph nodes (Fig. 4B and C). The effective accumulation of DACHPt/m in the metastatic lymph nodes may account for their effective growth inhibition of lymphatic metastasis.

The *in vivo* distribution of fluorescent-labeled DACHPt/m was assessed by fluorescent imaging of the whole body of tumor-bearing mice. Twenty-four hours after intravenous injection of fluorescent-labeled DACHPt/m, intense fluorescence signal was detected at the tumor site, suggesting the selective accumulation of DACHPt/m in the orthotopic tumors (Fig. 5A). In addition, mice were sacrificed and the tumor, metastatic lymph nodes and organs (i.e., spleen, liver and kidneys) were imaged *ex vivo* (Fig. 5B). The high fluorescence signal of the micelles in the tumor and metastatic lymph nodes indicates the ability of the micelles to target the scirrhous gastric tumors and their lymphatic metastases.

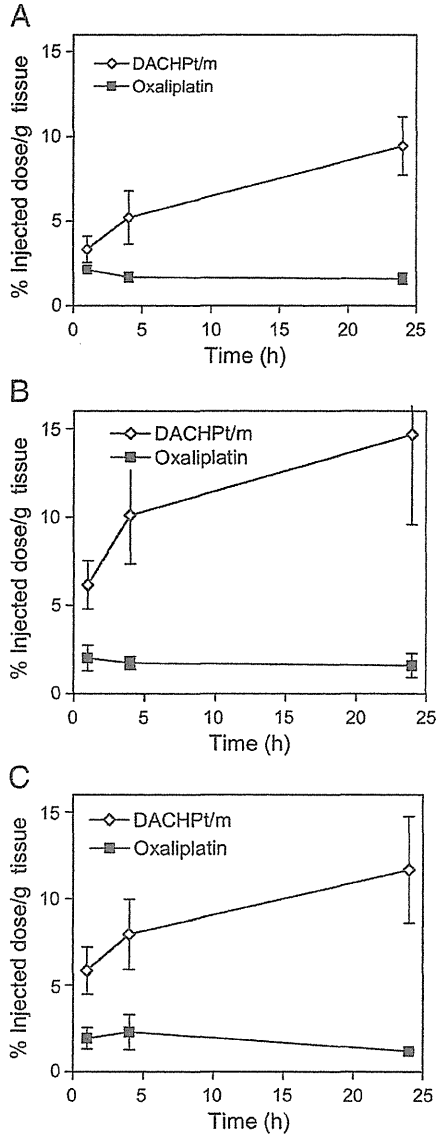

Fig. 4. Accumulation of oxaliplatin and DACHPt/m in OCUM-2-MLN-Luc orthotopic tumors and lymph node metastasis. A, Orthotopic tumor. B, Primary metastatic lymph node (sentinel lymph node). C, Secondary metastatic lymph node. Data are expressed as a mean ± SE ($n = 5$).

3.5. Microdistribution of fluorescent-labeled DACHPt/m in orthotopic tumors and metastastic lymph nodes

Firstly, the histology of OCUM-2MLN tumors was examined by H&E staining (Fig. 6A). These tumors present poorly differentiated characteristics with hypovascularity and extensive stromal fibrosis of gastric cancers [9]. The microdistribution of the fluorescent-labeled DACHPt/m in the tissue sections of the orthotopic gastric tumors was assessed by fluorescence microscopy. The nucleus of the cells in the whole tissue sections were stained with Hoechst (Fig. 6B, blue) while the tumors regions were stained by using anti-CD326 antibody (Fig. 6B, green), which recognizes the human epithelial antigen (HEA). The colocalization of the fluorescent-labeled DACHPt/m (Fig. 6B, magenta) with the CD326-stained cancer cells (Fig. 6B, green) suggests the homogeneous accumulation of the micelles in the tumor tissue (Fig. 6B). Moreover, the blood vessels, marked with anti-PECAM-1 antibody, were not detectable within the tumor (Fig. 6C, green), suggesting the hypovascular nature of the tumors. Also, the lymphatic vessels, marked with anti-LIVE-1 antibody, were not detected inside the tumor tissue (Fig. 6C, blue). In OCUM-2MLN tumor model, the cancer cells exhibit tumor invasion into peritumoral lymphatic vessels and spread along the lymphatic vessels in the gastric wall to the regional lymph nodes [33]. The fluorescence of the micelles was detected in the tumor sections even at the regions distant from the blood vessels (Fig. 6C, magenta), suggesting the deep penetration of DACHPt/m within the tumor tissue.

The H&E staining of the metastatic lymph nodes (Fig. 7A) indicated the abnormal anatomy of the lymph node due to the tumor growth. Fluorescent signal from the micelles was found to be colocalized with cancer cells, stained by CD326, in the metastatic lymph nodes, suggesting that micelles deeply penetrate into the metastases in the lymph nodes (Fig. 7B). Additionally, the lymphatic tissue and blood vessels were stained with anti-LYVE-1 and anti-PECAM-1 antibodies, respectively (Fig. 7C). LYVE-1-positive lymphatic tissue was mainly found in the periphery of the tumor in the lymph node (Fig. 7C, blue). Fluorescent-labeled micelles were found to accumulate within the tumoral region of the metastatic lymph nodes (Fig. 7C, magenta).

It is assumed that polymeric micelles from the circulation may reach the lymph nodes either through the lymphatic vessels or blood vessels. Meanwhile, the fluorescent micelles were not detected in healthy lymph nodes (Supplementary Fig. S4). The histological examinations of the enhanced accumulation of DACHPt/m in the metastatic lymph nodes are quite consistent with the significant growth inhibition of lymph node metastasis observed in DACHPt/m treated animals (Fig. 3).

4. Discussion

In the present study, we examined the targeting ability of DACHPt/m against the orthotopic model of scirrhous gastric cancer (SGC) from OCUM-2MLN cells, which is accompanied with very high rate of lymph node metastasis [30–31]. The metastasis to the lymph nodes is an important indicator for the staging of SGC and a determinant for the prognosis [35–36]. Here, we have successfully demonstrated that systemically administered DACHPt/m can target both orthotopic scirrhous gastric tumors and their lymphatic metastasis, achieving a remarkable inhibitory effect on their growth.

The biodistribution study revealed that the micelles significantly accumulated in the tumors and the metastatic lymph nodes (Figs. 5 and 6) while showing appreciably lower accumulation in organs or healthy lymph nodes (Fig. **5** and Fig.**S4**). The accumulation of DACHPt/m in the orthotopic OCUM-2MLN tumors might be related to the passive targeting based on the EPR effect. However, we have previously reported that doxorubicin-loaded polymeric micelles with 65-nm diameter showed poor accumulation and reduced efficacy against orthotopic OCUM-2MLN tumors [9]. Regarding such discrepancy, we assume that a relatively small size (30 nm) of DACHPt/m should be important for effective extravasation and tumor penetration in orthotopic OCUM-2MLN tumors. Recently, we have studied the size effect of DACHPt/m in subcutaneous human pancreatic adenocarcinoma BxPC3 tumors [29], which share histological characteristics with OCUM-2MLN tumors, such as sparse formation of blood vessels and very thick fibrotic stroma [30–31]. Accordingly, DACHPt/m with 30-nm diameter effectively extravasated and penetrated in the pancreatic tumors while DACHPt/m with diameter larger than 50-nm remained in the perivascular areas of the tumors [29]. Based on these observations, we preliminarily studied the size effect of DACHPt/m in an orthotopic OCUM-2MLN tumor model in this study (Supplementary Information). As shown in Supplementary Fig. **S3**, 30-nm DACHPt/m showed potent antitumor efficacy and enhanced tumor accumulation against gastric tumors, whereas 70-nm DACHPt/m failed to exhibit significant antitumor effect and showed

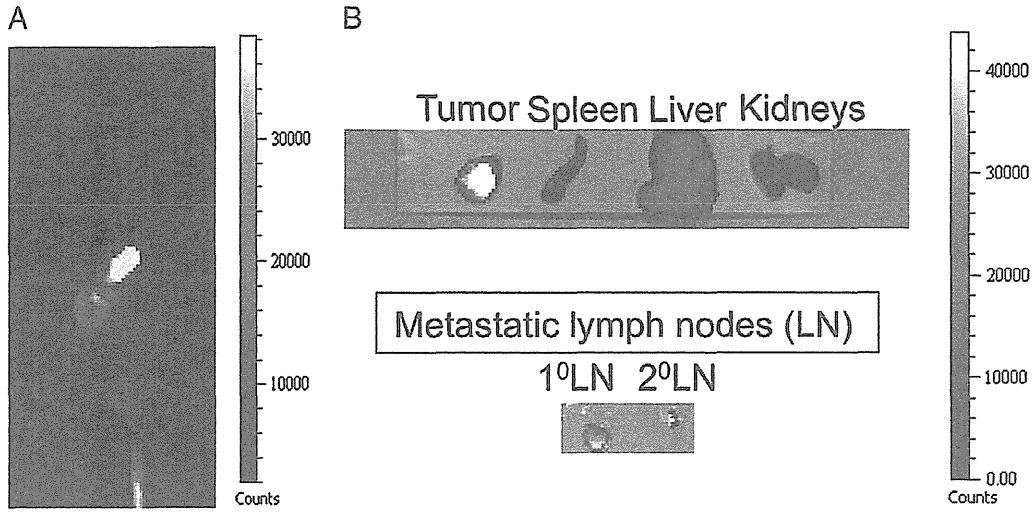

Fig. 5. Biodistribution of Alexa 680-labeled DACHPt/m. A, Whole body near infrared (NIR) fluorescent image of orthotopic OCUM-2-MLN-Luc tumor-bearing mouse 24 h after the injection of Alexa 680-labeled DACHPt/m. The micelles are detected specifically at the tumor site. B, *Ex vivo* fluorescent imaging of orthotopic tumor, organs and metastatic lymph nodes.

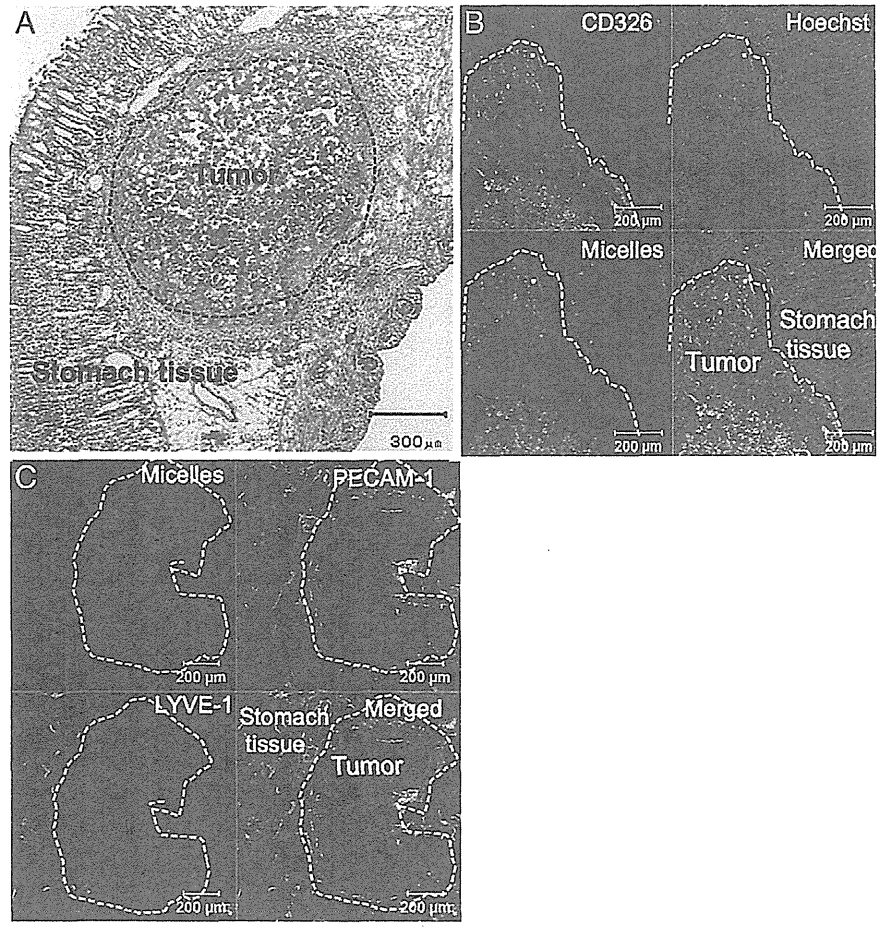

Fig. 6. Histological analysis of orthotopic OCUM-2-MLN-Luc and microdistribution of fluorescent labeled DACHPt/m. A, H&E staining of orthotopic OCUM-2-MLN-Luc tumor sections. B, Immunofluorescence microscopy of gastric cancer cells (CD326, green) and Alexa 594-labeled DACHPt/m (magenta) in orthotopic OCUM-2-MLN-Luc tumors. The cells nuclei were stained with Hoechst 33342 (blue). C, Microdistribution of Alexa 594-labeled DACHPt/m (micelles, magenta), blood vessels (PECAM-1, green) and lymphatic vessels (LYVE-1, blue) in orthotopic OCUM-2-MLN-Luc tumors determined by immunofluorescence microscopy.

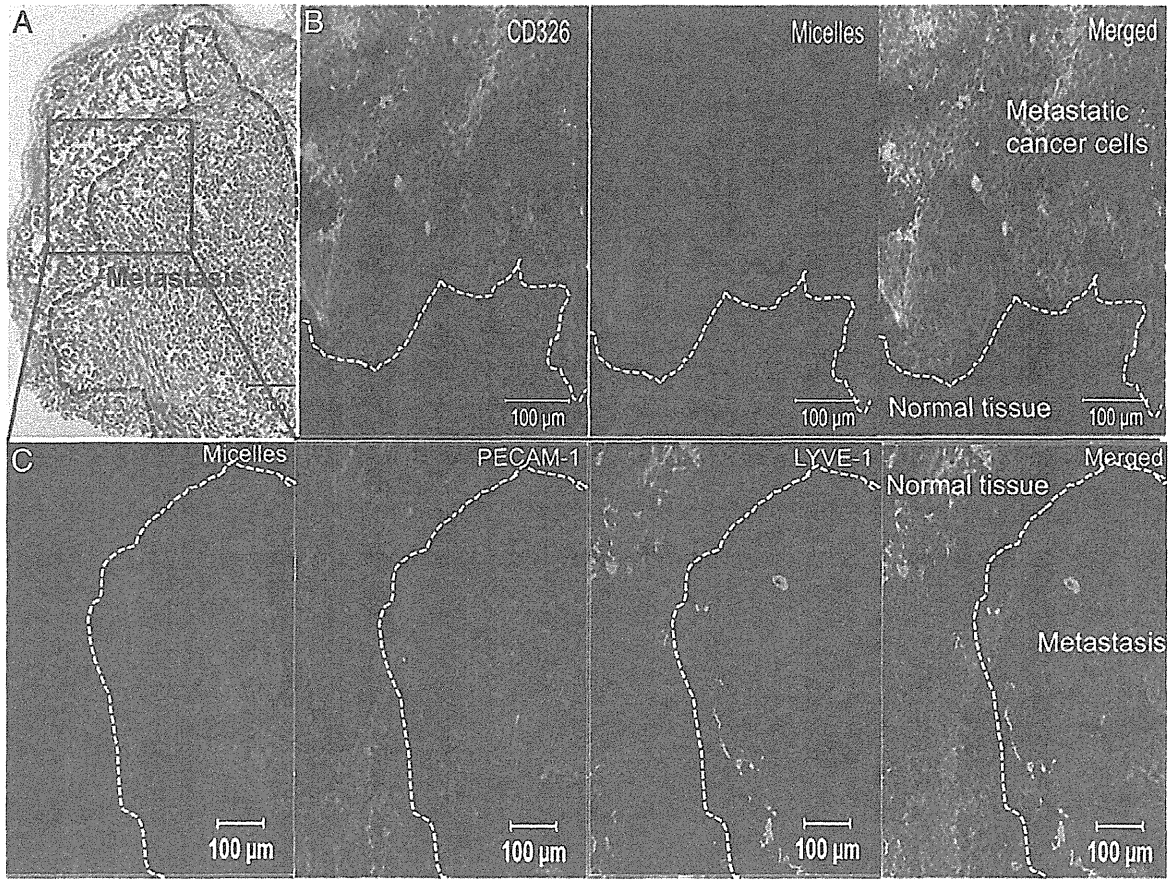

Fig. 7. Histological analysis of metastatic lymph nodes and microdistribution of fluorescent labeled DACHPt/m. A, H&E staining of metastatic lymph node. B, Immunofluorescence microscopy of gastric cancer cells (CD326, green) and Alexa 594-labeled DACHPt/m (micelles, magenta) in the metastatic lymph nodes. C, Microdistribution of Alexa 594-DACHPt/m (micelles, magenta), blood vessels (PECAM-1, green) and lymphatic vessels (LYVE-1, blue) in metastatic lymph nodes (Inset of A) determined by immunofluorescence microscopy.

poor tumor accumulation. These results are consistent with the aforementioned assumption that effective properties of DACHPt/m against a scirrhous gastric cancer model may be attributed to their relatively small size.

The observation of DACHPt/m accumulation into the fibrous OCUM-2MLN tumor here is apparently consistent with the scheme of EPR effect. On the other hand, the mechanisms of the accumulation of the micelles in the metastatic lymph nodes remain to be clarified yet. Two mechanisms for the accumulation of the micelles in the metastatic lymph nodes may be proposed: (i) the micelles accumulate in the orthotopic tumors, followed by migration and accumulation in the metastatic lymph nodes via the lymphatic vessels, (ii) the micelles can directly accumulate in the metastatic lymph nodes via blood vessels in the metastatic niche probably due to the enhanced permeability of these blood vessels. Regarding the former mechanism, intratumorally-injected nanocarriers have been demonstrated to accumulate in the metastatic lymph nodes [16,17,37,38]. Also, Harisinghani et al. reported in patients that systemically injected superparamagnetic iron oxide nanoparticles (SPION) accumulate in the metastatic lymph nodes [39]. This phenomenon was explained by accumulation of SPION in solid tumors, followed by their uptake by tumor macrophages, which migrate to metastatic lymph nodes [39]. The detailed mechanisms underlying the accumulation of the micelles in the metastatic lymph nodes are under investigation and will be reported elsewhere.

The targeting capability of the micelles to scirrhous gastric tumors and their metastatic lymph nodes could be applied not only for treatment but also for diagnosis. A variety of contrast agents, including fluorescent probes, MRI or PET contrast agents [5] can be incorporated into the micellar structure. Thus, primary scirrhous tumors and nodal involvement may be directly observed by non-invasive imaging. Moreover, the combination of therapy and imaging within single micelles may allow the evaluation of the therapeutic response, offering an emerging concept of theranostic nanomedicines [5,27].

In conclusion, our results highlight that systemically injected DACHPt/m can extravasate and penetrate in orthotopic scirrhous gastric tumors and lymph node metastasis, eliciting significantly potent antitumor activity. Enhanced drug delivery to the lymph node metastasis by polymeric micelles can improve the morbidity of the patients with SGC. DACHPt/m can also be useful for the adjuvant therapy of SGC, that is, the administration of the micelles before surgery, by improving the lymph node status while controlling the tumor volume, which may lead to the downgrading of unresectable scirrhous gastric cancer. Moreover, control of distant lymph node metastasis by DACHPt/m can impede further dissemination of the disease. Our findings suggest the high potential of systemically administered nanocarriers for the treatment of scirrhous gastric cancer as well as lymph node metastasis.

Acknowledgments

This study was supported by Funding Program for World-Leading Innovative R&D on Science and Technology (FIRST Program) from the Japan Society for the Promotion of Science (JSPS) and Grants-in-Aid

for Scientific Research from the Japanese Ministry of Health, Labour, and Welfare (MHLW).

Appendix A. Supplementary data

Supplementary data to this article can be found online at doi:10.1016/j.jconrel.2012.01.038.

References

[1] R. Duncan, The dawning era of polymer therapeutics, Nat. Rev. Drug Discov. 2 (2003) 347–360.
[2] M.E. Davis, Z. Chen, D. Shin, Nanoparticle therapeutics: an emerging treatment modality for cancer, Nat. Rev. Drug Discov. 7 (2008) 771–782.
[3] K. Kataoka, A. Harada, Y. Nagasaki, Block copolymer micelles for drug delivery: design, characterization and biological significance, Adv. Drug Deliv. Rev. 47 (2001) 113–131.
[4] N. Nishiyama, K. Kataoka, Current state, achievements, and future prospects of polymeric micelles as nanocarriers for drug and gene delivery, Pharmacol. Ther. 112 (2006) 630–648.
[5] H. Cabral, N. Nishiyama, K. Kataoka, Supramolecular nanodevices: from design validation to theranostic nanomedicine, Acc. Chem. Res. 44 (2011) 999–1008.
[6] Y. Matsumura, H. Maeda, A new concept for macromolecular therapeutics in cancer chemotherapy: mechanism of tumoritropic accumulation of proteins and the antitumor agent Smancs, Cancer Res. 46 (1986) 6387–6392.
[7] J.J. Gottlieb, K. Washenik, A. Chachoua, A. Friedman-Kien, Treatment of classic Kaposi's sarcoma with liposomal encapsulated doxorubicin, Lancet 350 (1997) 1363–1364.
[8] W.J. Gradishar, S. Tjulandin, N. Davidson, H. Shaw, N. Desai, P. Bhar, M. Hawkins, J. O'Shaughnessy, Phase III trial of nanoparticle albumin-bound paclitaxel compared with polyethylated castor oil-based paclitaxel in women with breast cancer, J. Clin. Oncol. 23 (2005) 7794–7803.
[9] M.R. Kano, Y. Bae, C. Iwata, Y. Morishita, M. Yashiro, M. Oka, T. Fujii, A. Komuro, K. Kiyono, M. Kaminishi, K. Hirakawa, Y. Ouchi, N. Nishiyama, K. Kataoka, K. Miyazono, Improvement of cancer-targeting therapy, using nanocarriers for intractable solid tumors by inhibition of TGF-β signaling, Proc. Natl. Acad. Sci. U. S. A. 104 (2007) 3460–3465.
[10] M.R. Kano, Y. Komuta, C. Iwata, M. Oka, Y.T. Shirai, Y. Morishita, Y. Ouchi, K. Kataoka, K. Miyanozo, Comparison of the effects of the kinase inhibitors imatinib, sorafenib, and transforming growth factor-β receptor inhibitor on extravasation of nanoparticles from neovasculature, Cancer Sci. 100 (2009) 173–180.
[11] K.D. Crew, A.I. Neugut, Epidemiology of gastric cancer, World J. Gastroenterol. 12 (2006) 354–362.
[12] E. Otsuji, Y. Kuriu, K. Okamoto, T. Ochiai, D. Ichikawa, A. Hagiwara, H. Yamagishi, Outcome of surgical treatment for patients with scirrhous carcinoma of the stomach, Am. J. Surg. 188 (2004) 327–332.
[13] Japanese Gastric, Cancer A Japanese classification of gastric carcinoma—2nd English Edition, Gastric Cancer 1 (1998) 10–24.
[14] Y. Hippo, M. Yashiro, M. Ishii, H. Taniguchi, S. Tsutumi, K. Hirakawa, T. Kosama, H. Aburatani, Differential gene expression profiles of scirrhous gastric cancer cells with high metastatic potential to peritoneum or lymph nodes, Cancer Res. 61 (2001) 889–895.
[15] Y. Maehara, Y. Emi, H. Baba, Y. Adachi, K. Akazawa, Y. Ichiyoshi, K. Sugimachi, Recurrences and related characteristics of gastric cancer, Br. J. Cancer 74 (1996) 975–979.
[16] A. Hagiwara, T. Takahashi, K. Sawai, C. Sakakura, M. Shirasu, M. Ohgaki, T. Imanishi, J. Yamasaki, Y. Takemoto, N. Kageyama, Selective drug delivery to peri-tumoral region and regional lymphatics by local injection of aclarubicin adsorbed on activated carbon particles in patients with breast cancer—a pilot study, Anticancer Drugs 8 (1997) 666–670.
[17] C. Oussoren, G. Storm, Liposomes to target the lymphatics by subcutaneous administration, Adv. Drug Deliv. Rev. 50 (2001) 143–156.
[18] P. Hirnle, Targeted introduction of substances into the lymph nodes for endolymphatic therapy, in: Stanley P.L. Leong (Ed.), Cancer metastasis and the lymphovascular system: basis for rational therapy, Springer, 2007, p. 101.
[19] K. Yamagata, K. Kumagai, K. Shimizu, K. Masuo, Y. Nishida, A. Yasui, Gastrointestinal cancer metastasis and lymphogenous spread: viewpoint of animal models of lymphatic obstruction, Jpn. J. Clin. Oncol. 28 (1998) 104–106.
[20] Y. Matsumura, T. Hamaguchi, T. Ura, K. Muro, Y. Yamada, Y. Shimada, K. Shirao, T. Okusaka, H. Ueno, M. Ikeda, N. Watanabe, Phase I clinical trial and pharmacokinetic evaluation of NK911, a micelle-encapsulated doxorubicin, Br. J. Cancer 91 (2004) 1775–1781.
[21] T. Hamaguchi, K. Kato, H. Yasui, C. Morizane, M. Ikeda, H. Ueno, K. Muro, Y. Yamada, T. Okusuka, K. Shirao, Y. Shimada, H. Nakahama, Y. Matsumura, A phase I and pharmacokinetic study of NK105, a paclitaxel-incorporating micellar nanoparticle formulation, Br. J. Cancer 97 (2007) 170–176.
[22] Y. Matsumura, K. Kataoka, Preclinical and clinical studies of anticancer agent-incorporating polymer micelles, Cancer Sci. 100 (2009) 572–579.
[23] Y. Matsumura, Preclinical and clinical studies of NK012, an SN-38-incorporating polymeric micelles, which is designed based on EPR effect, Adv. Drug Deliv. Rev. 63 (2010) 184–192.
[24] R. Plummer, R.H. Wilson, H. Calvert, A.V. Boddy, M. Griffin, J. Sludden, M.J. Tilby, M. Eatock, D.G. Pearson, C.J. Ottley, Y. Matsumura, K. Kataoka, T. Nishiya, A Phase I clinical study of cisplatin-incorporated polymeric micelles (NC-6004) in patients with solid tumours, Br. J. Cancer 104 (2011) 593–598.
[25] H. Cabral, N. Nishiyama, S. Okazaki, H. Koyama, K. Kataoka, Preparation and biological properties of dichloro(1,2-diaminocyclohexane)platinum (II) (DACHPt)-loaded polymeric micelles, J. Control. Release 101 (2005) 223–232.
[26] H. Cabral, N. Nishiyama, K. Kataoka, Optimization of (1,2-diamino-cyclohexane) platinum(II)-loaded polymeric micelles directed to improved tumour targeting and enhanced antitumour activity, J. Control. Release 121 (2007) 146–155.
[27] S. Kaida, H. Cabral, M. Kumagai, A. Kishimura, Y. Terada, M. Sekino, I. Aoki, N. Nishiyama, T. Tani, K. Kataoka, Visible drug delivery by supramolecular nanocarriers directing to single-platformed diagnosis and therapy of pancreatic tumor model, Cancer Res. 70 (2010) 7031–7041.
[28] M. Murakami, H. Cabral, Y. Matsumoto, S. Wu, M.R. Kano, T. Yamori, N. Nishiyama, K. Kataoka, Improving drug potency and efficacy by nanocarrier-mediated subcellular targeting, Sci. Transl. Med. 3 (2011) 64ra2.
[29] H. Cabral, Y. Matsumoto, K. Mizuno, Q. Chen, M. Murakami, M. Kimura, Y. Terada, M.R. Kano, K. Miyazono, M. Uesaka, N. Nishiyama, K. Kataoka, Accumulation of sub-100nm polymeric micelles in poorly permeable tumours depends on size, Nat. Nanotech. 6 (2011) 815–823.
[30] T. Fujihara, T. Sawada, K. Hirakawa, Y.S. Chung, M. Yashiro, T. Inoue, M. Sowa, Establishment of lymph node metastatic model for human gastric cancer in nude mice and analysis of factors associated with metastasis, Clin. Exp. Metastasis 16 (1998) 389–398.
[31] M. Yashiro, K. Hirakawa, Cancer–stromal interactions in scirrhous gastric carcinoma, Cancer Microenviron. 3 (2010) 127–135.
[32] K. Shibuya, J. Shirakawa, T. Kameyama, S. Honda, S. Tahara Hanaoka, A. Miyamoto, M. Onodera, T. Sumida, H. Nakauchi, H. Miyoshi, A. Shibuya, CD226 (DNAM-1) is involved in lymphocyte function-associated antigen 1 costimulatory signal for naive T cell differentiation and proliferation, J. Exp. Med. 198 (2003) 1829–1839.
[33] C. Iwata, M.R. Kano, A. Komuro, M. Oka, K. Kiyono, E. Johansson, Y. Morishita, M. Yashiro, K. Hirakawa, M. Kaminishi, K. Miyazono, Inhibition of cyclooxygenase-2 suppresses lymph node metastasis via reduction of lymphangiogenesis, Cancer Res. 67 (2007) 10181–10189.
[34] D.E. Jenkins, Y. Oei, Y.S. Hornig, S.F. Yu, J. Dusich, T. Purchio, P.R. Contag, Bioluminescent imaging (BLI) to improve and refine traditional murine models of tumor growth and metastasis, Clin. Exp. Metastasis. 20 (2003) 733–744.
[35] M.S. Karpeh, L. Leon, D. Klimstra, M.F. Brennan, Lymph node staging in gastric cancer: is location more important than Number? An analysis of 1,038 patients, Ann. Surg. 232 (2000) 362–371.
[36] C.Y. Chen CY, C.W. Wu, S.S. Lo, M.C. Hsieh, W.Y. Lui, K.H. Shen, Peritoneal carcinomatosis and lymph node metastasis are prognostic indicators in patients with Borrmann type IV gastric carcinoma, Hepatogastroenterology 49 (2002) 874–877.
[37] C. Oussoren, G. Storm, Lymphatic uptake and biodistribution of liposomes after subcutaneous injection: III. Influence of surface modification with poly(ethyleneglycol), Pharm. Res. 14 (1997) 1479–1484.
[38] G. Luo, X. Yu, C. Jin, F. Yang, D. Fu, J. Long, J. Xu, C. Zhan, W. Lu, LyP-1-conjugated nanoparticles for targeting drug delivery to lymphatic metastatic tumors, Int. J. Pharm. 385 (2010) 150–156.
[39] M.G. Harisinghani, J. Barentsz, P.F. Hahn, W.M. Deserno, S. Tabatabaei, C.H. van de Kaa, J. de la Rosette, R. Weissleder, Noninvasive detection of clinically occult lymph-node metastases in prostate cancer, N. Engl. J. Med. 348 (2003) 2491–2499.

Biomaterials 34 (2013) 492–500

Contents lists available at SciVerse ScienceDirect

Biomaterials

journal homepage: www.elsevier.com/locate/biomaterials

Gd-DTPA-loaded polymer–metal complex micelles with high relaxivity for MR cancer imaging

Peng Mi [a], Horacio Cabral [a], Daisuke Kokuryo [b], Mohammad Rafi [c], Yasuko Terada [d], Ichio Aoki [b], Tsuneo Saga [b], Ishii Takehiko [a], Nobuhiro Nishiyama [c,**], Kazunori Kataoka [a,c,e,*]

[a] Department of Bioengineering, Graduate School of Engineering, The University of Tokyo, 7-3-1 Hongo, Bunkyo-ku, Tokyo 113-8656, Japan
[b] Molecular Imaging Center, National Institute of Radiological Sciences, Anagawa 4-9-1, Inage, Chiba 263-8555, Japan
[c] Center for Disease Biology and Integrative Medicine, Graduate School of Medicine, The University of Tokyo, 7-3-1 Hongo, Bunkyo-ku, Tokyo 113-0033, Japan
[d] SPring 8, JASRI, 1-1-1 Kouto, Sayo-cho, Sayo-gun, Hyogo 679-5198, Japan
[e] Department of Materials Engineering, Graduate School of Engineering, The University of Tokyo, 7-3-1 Hongo, Bunkyo-ku, Tokyo 113-8656, Japan

ARTICLE INFO

Article history:
Received 12 July 2012
Accepted 16 September 2012
Available online 8 October 2012

Keywords:
Micelles
Drug delivery
Magnetic resonance imaging (MRI)
Polymer-metal complex
Cancer diagnosis

ABSTRACT

Nanodevices for magnetic resonance imaging of cancer were self-assembled to core–shell micellar structures by metal complex formation of K_2PtCl_6 with diethylenetriaminepentaacetic acid gadolinium (III) dihydrogen (Gd-DTPA), a T_1-contrast agent, and poly(ethylene glycol)-*b*-poly{N-[N′-(2-aminoethyl)-2-aminoethyl]aspartamide} (PEG-*b*-PAsp(DET)) copolymer in aqueous solution. Gd-DTPA-loaded polymeric micelles (Gd-DTPA/m) showed a hydrodynamic diameter of 45 nm and a core size of 22 nm. Confining Gd-DTPA inside the core of the micelles increased the relaxivity of Gd-DTPA more than 13 times (48 mM^{-1} s^{-1}). In physiological conditions Gd-DTPA/m sustainedly released Gd-DTPA, while the Pt(IV) complexes remain bound to the polymer. Gd-DTPA/m extended the circulation time in plasma and augmented the tumor accumulation of Gd-DTPA leading to successful contrast enhancement of solid tumors. μ-Synchrotron radiation-X-ray fluorescence results confirmed that Gd-DTPA was delivered to the tumor site by the micelles. Our study provides a facile strategy for incorporating contrast agents, dyes and bioactive molecules into nanodevices for developing safe and efficient drug carriers for clinical application.

1. Introduction

Early detection of neoplastic lesions is critical for success in cancer therapy. Magnetic resonance imaging (MRI) provides a powerful diagnostic imaging modality of cancer, because of its non-invasiveness, high definition and precise three-dimensional positioning ability [1,2]. Paramagnetic compounds are widely used as MRI contrast agents (CAs) to amplify the signals of MRI tomography and improve the contrast between magnetic similar but histological dissimilar tissues [3,4]. Several low molecular weight paramagnetic complexes of gadolinium(III) are used for clinical MRI as they can decrease the longitudinal relaxation time T_1 of surrounding water protons [5–7]. Among these complexes, Gd-DTPA, one of the most commonly used T_1-contrast agent for clinical MRI, is featured by high thermodynamic and kinetic stabilities, which reduce the release of toxic Gd^{3+} ions, besides a longitudinal relaxivity, r_1, of ~3.5 mM^{-1} s^{-1} at 1.4 T [3,5,7]. Nevertheless, the inherent low relaxivity, short circulation time in blood and low specificity to tissues limit its applications. From this viewpoint, high relaxivity CAs with promoted tissue detection and hindered release of free Gd^{3+} ions are required to improve the performance of imaging.

Nanodevices have been recently developed to selectively deliver imaging agents to solid tumors by leaking out from circulation due to the enhanced permeability of the tumor vasculature [8–12]. In this way, macromolecules, liposomes, dendrimers and nanoparticles carrying high payloads of CAs have been developed to enhance the MR contrast of solid tumors [13–25]. In most cases, Gd-based CAs were covalently incorporated to the structures of nanocarriers to increase the bloodstream circulation, the tumor accumulation and, in some cases, the relaxivity of the loaded CAs

* Corresponding author. Department of Bioengineering, Graduate School of Engineering, The University of Tokyo, 7-3-1 Hongo, Bunkyo-ku, Tokyo 113-8656, Japan. Tel.: +81 3 5841 7138; fax: +81 3 5841 7139.
** Corresponding author. Tel./fax: +81 3 5841 1430.
E-mail addresses: nishiyama@bmw.t.u-tokyo.ac.jp (N. Nishiyama), kataoka@bmw.t.u-tokyo.ac.jp (K. Kataoka).

0142-9612/$ – see front matter © 2012 Elsevier Ltd. All rights reserved.
http://dx.doi.org/10.1016/j.biomaterials.2012.09.030

[14,22,23]. Nevertheless, covalent binding of Gd-chelates to macromolecular systems may increase the risk of Gd^{3+} ion leakage from the chelates due to the prolonged half-life in the body and cumulative toxicity [26]. Thus, the design of tumor-targeted nanodevices for Gd-based CAs should consider such issues for constructing safe carriers, which could target the tumor position and release Gd-DTPA easily from nanodevices.

Among promising nanodevice systems for MRI, block copolymeric micelles, i.e. nanostructures consisting of a drug-loaded core and poly(ethylene glycol) (PEG) protective shell, present exceptional advantages including their relatively small sizes, ability to engineer drug loading mechanisms, controlled release of their cargo, prolonged life in the bloodstream and enhanced accumulation in solid tumors after intravenous administration [19–25]. Auspicious results from clinical trials of micelle formulations incorporating anticancer agents indicate the potential clinical application of polymeric micelles [27,28].

The aim of this study was to develop core–shell type micellar nanocarriers of Gd-DTPA for tumor imaging, which can incorporate Gd-DTPA via the reversible Pt-Gd-DTPA complexation, allowing sustained release of free Gd-DTPA in biological environments. In order to incorporate hydrophilic low molecular weight paramagnetic complexes Gd-DTPA into polymeric micelle, we utilized Pt(IV) ions to "cross-link" carboxyl groups of Gd-DTPA to amino groups of PEG-*b*-PAsp(DET) copolymers. Gd-DTPA/m could passively accumulate in solid tumors due to the enhanced permeability and retention (EPR) effect. Thus, the improved tumor accumulation of Gd-DTPA could enhance the T_1 weighed contrast of the malignancies in mice. Otherwise, in physiological environments such as plasma, the ligand exchange reaction of Pt(IV) from the carboxylic group of Gd-DTPA to chloride ions results in sustained release of free Gd-DTPA, which can be rapidly cleared from the body via glomerular excretion.

2. Materials and methods

2.1. Materials

α-Benzyl-L-aspartate *N*-carboxy anhydride (BLA-NCA) was obtained from Chuo Kaseihin Co., Inc. (Tokyo, Japan). Poly(ethylene glycol) (MeO-PEG-NH_2) (M_w = 12,000, M_w/M_n = 1.03) were purchased Nippon Oil and Fats Co., Ltd. (Tokyo, Japan). Benzene, *N*,*N*-dimethylformamide (DMF), *n*-butylamine, dichloromethane (CH_2Cl_2), diethylenetriamine (DET), potassium hexachloroplatinate(IV) (K_2PtCl_6) and *N*-methyl-2-pyrrolidone (NMP) were purchased from Wako Pure Chemical Industries (Osaka, Japan) and distilled by a general method before use. Arsenazo III and Gd-DTPA were purchased from Aldrich Chemical (Milwaukee, USA), and then Gd-DTPA was converted to sodium salt by adjusting the pH to 7 with NaOH and lyophilization. 400-mesh copper grids were obtained from Nisshin E. M. Spectra/Por-6 membrane was purchased from Spectrum Laboratories (Rancho Dominguez, CA). Dulbecco's modified eagle's medium (DMEM) was obtained from Sigma–Aldrich Co. (St. Louis, USA). Fetal bovine serum (FBS) was purchased from MP Biomedicals, Inc. (Illkirch, France). 96-well culture plates were purchased from Becton Dickinson Labware (Franklin Lakes, USA). The Cell Counting Kit-8 was purchased from Dojindo Laboratories (Kumamoto, Japan).

Murine colon adenocarcinoma 26 (C-26) cells were kindly supplied by the National Cancer Center (Tokyo, Japan). Human umbilical vein endothelial cells (HUVEC), and the endothelial cell growth medium-2 bullet kit (EGM-2 bullet kit) were obtained from Lonza Ltd. (Basel, Switzerland). B16-F10 melanoma cells were purchased from the American Type Culture Collection (Virginia, USA). All the cells are maintained with medium in a humidified atmosphere containing 5% CO_2 at 37 °C. CDF_1 mice (female; 18–20 g body weight; 6 weeks old) were purchased from Charles River Japan (Kanagawa, Japan) and, treated following the policies of the Animal Ethics Committee of the University of Tokyo.

2.2. Synthesis of PEG-b-PAsp(DET)

As shown in Scheme S1, poly(ethylene glycol)-*b*-poly(β-benzyl L-aspartate) (PEG-*b*-PBLA) with different degree of polymerization (DP) (DP = 25, 35, 45) were synthesized by ring-opening polymerization of BLA-NCA initiated by MeO-PEG-NH_2 (M_w = 12,000) according to previously reported method with minor modification [29]. Briefly, BLA-NCA (1.1 g, 4.5 mmol) was dissolved in DMF (2 mL) and then diluted with CH_2Cl_2 (20 mL). MeO-PEG-NH_2 (1.2 g, 0.1 mmol) dissolved in CH_2Cl_2 was added to the solution of BLA-NCA. The reaction was carried out with stirring for 2 days at 35 °C. All the procedures above were under dry argon protection. PEG-*b*-PBLA was collected by precipitating in excess amount of diethyl ether, filtration and vacuumed to dry. In Figure S1, the ^1H NMR spectrum of PEG-*b*-PBLA was measured in d_6-DMSO at 80 °C with a JEOL EX300 spectrometer (JEOL, Tokyo, Japan) using tetramethylsilane (TMS) as an internal standard, and the degree of polymerization (DP = 25, 35, 45) was calculated from the peak intensity ratio of protons both in phenyl groups of PBLA ($C_6H_5CH_2$–, δ = 7.3 ppm) and methylene units (–CH_2CH_2–, δ = 3.6 ppm) of PEG. The polydispersity of PEG-*b*-PBLA was characterized by gel permeation chromatography (GPC) system (HLC-8220, TOSOH Co., Japan) equipped with TSK-gel columns (TOSOH Co., Tokyo, Japan) and an internal refractive index (RI) detector at 40 °C. NMP containing 50 mM LiBr was used as mobile phase with a flow rate of 0.35 mL/min and linear PEG standards were used for calibration. As shown in Figure S2, the GPC chromatogram of the prepared PEG-*b*-PBLA has a unimodal molecular weight distribution (M_w/M_n: 1.03).

PEG-*b*-PAsp(DET) with different DP (25, 35, 45) were prepared separately via aminolysis reaction of PEG-*b*-PBLA with DET following the protocol modified from our former reported method [30]. Briefly, lyophilized PEG-*b*-PBLA (200 mg, 0.01 mmol) was dissolved in NMP (2 mL) and maintained at 5 °C. DET (2.3 mL, 50-equivalent to BLA) was diluted with NMP (2.3 mL) and kept at 5 °C. PEG-*b*-PBLA was added to DET solution and reacted with stirring at 5 °C for 1 h. The reacted mixture was neutralized by 5 M HCl aqueous solution (13 mL, equivalent to the added amino groups) in an ice bath, then dialysis (MWCO: 6000–8000) against 0.01 M HCl aqueous solution, then dialyzed with Milli-Q water under 4 °C. PEG-*b*-PAsp(DET) as the chloride salt form was collected via freeze-dry of final solution. ^1H NMR (D_2O) measurement showed the disappearance of signals belonging to the benzyl group and all the signals featured with PEG-*b*-PAsp(DET) (Figure S3). Degree of polymerization (DP = 25, 35, 45) was calculated by comparing the peak intensity ratio between methylene protons of the α, β-Asp segment (peak f, δ = 2.8 ppm) and methylene units (–CH_2CH_2–, δ = 3.6 ppm) of PEG. GPC measurements of block copolymers were carried out utilizing a HPLC system (JASCO, Japan) equipped with Superdex 75 10/300 GL column (GE Healthcare UK, Ltd.) and UV detector set at 220 nm. The column was eluted with 10 mM AcOH buffer containing 500 mM NaCl (pH 7.4) at a flow rate of 0.5 mL/min at room temperature. The GPC chromatogram of the obtained PEG-*b*-PAsp(DET) was unimodal (Figure S4).

2.3. Preparation of Gd-DTPA-loaded micelles (Gd-DTPA/m)

K_2PtCl_6 (0, 1, 2.5, 5 and 10 mM) was dissolved in Milli-Q water adjusted to pH 7.4 using trace amount of NaOH or diluted in 5 mM PBS buffers, then mixed with Gd-DTPA (5 mM) to incubated at 37 °C for 24 h. PEG-*b*-PAsp(DET) (DP = 25, 35, 45; [DET] = 5 mM) was added to Pt/Gd-DTPA mixture ([Gd-DTPA]/[DET] = 1.0) and incubated at 4 °C for 120 h to spontaneously form Gd-DTPA loaded micelles (Gd-DTPA/m). The micelle was purified by dialysis (MWCO: 6000–8000) against Milli-Q water and ultrafiltration (MWCO: 30,000) to remove free drug and polymer in the solution. Size distribution of the Gd-DTPA/m was evaluated by dynamic light scattering (DLS) measurement at 25 °C using Zetasizer Nano ZS90 (Malvern Instruments, UK). The contents of platinum and gadolinium of micelles were determined by inductively coupled plasma-mass spectrometry (ICP-MS) (4500 ICP-MS; Hewlett Packard, USA).

2.4. Transmission electron microscopy (TEM)

The morphology of micelle was observed on a Transmission Electron Microscope (JEM-1400, JEOL, Japan) operated with 100 kv acceleration voltages and 40 uA beam current. Diluted micelle was stained by mixing with uranyl acetate solution (2%, w/v) and placed on 400-mesh copper grids. The diameters of the core of micelle and size distribution were calculated with Image J, which was designed and provided by National Institutes of Health (NIH). The elements distribution inside micelle was characterized using JEM-2100F (JEOL, Japan) under the scanning transmission electron microscopy (STEM) pattern and scanned by energy dispersive X-ray (EDX) spectra. The specimen for the elements measurements was prepared only loading micelle on 400-mesh copper grids without staining.

2.5. Arsenazo III colorimetric assay

Free Gd^{3+} was determined by the absorption of Gd-Arsenazo III complex referring one arsenazo III method [31]. Briefly, equal molar ratio of arsenazo III solution was mixed with of Gd-DTPA/K_2PtCl_6 mixtures, and then the absorbance spectra were measured using with an UV–vis spectrometer (V-570 UV/VIS/NIR Spectrophotometer, JASCO, Japan) at 660 nm. The absorbance of arsenazo III/$GdCl_3$, arsenazo III/Gd-DTPA, and arsenazo III were measured. All the solutions above were maintained at pH 7.4.

2.6. Release rate of Gd-DTPA from Gd-DTPA/m

The release characterization of Gd-DTPA from the micelle was evaluated by a dialysis method. 1 mL of Gd-DTPA/m solution and 1 mL PBS buffer (20 mM PBS with 300 mM NaCl) were put into dialysis bag (MWCO: 6000–8000) and

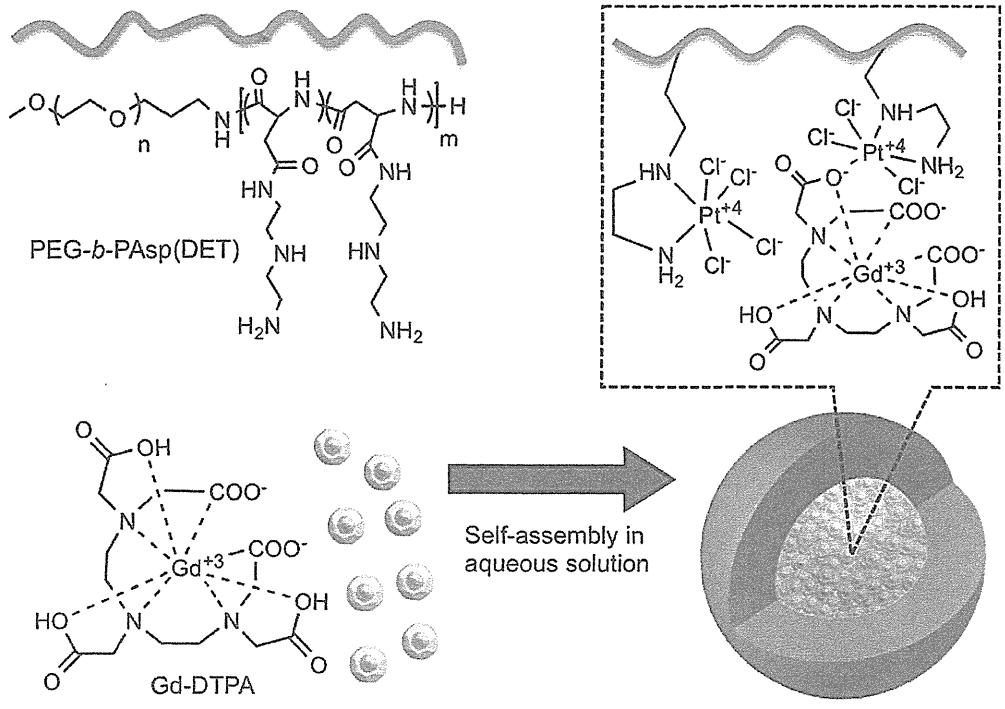

Scheme 1. Scheme illustration of the Gd-DTPA loaded micelle formation via polymer–metal complex formation.

incubated in 98 mL buffer of physiologic conditions (buffer: 10 mM PBS with 150 mM NaCl, temperature at 37 °C). 0.1 mL solution outside of the dialysis bag was sampled at defined time, and then the concentration of Gd-DTPA was measured by ICP-MS.

2.7. Characterization of r_1 relaxivity

The proton longitudinal relaxivity r_1, which is a parameter to evaluate the ability of contrast agents for MRI, can be determined from the change of the relaxation rate

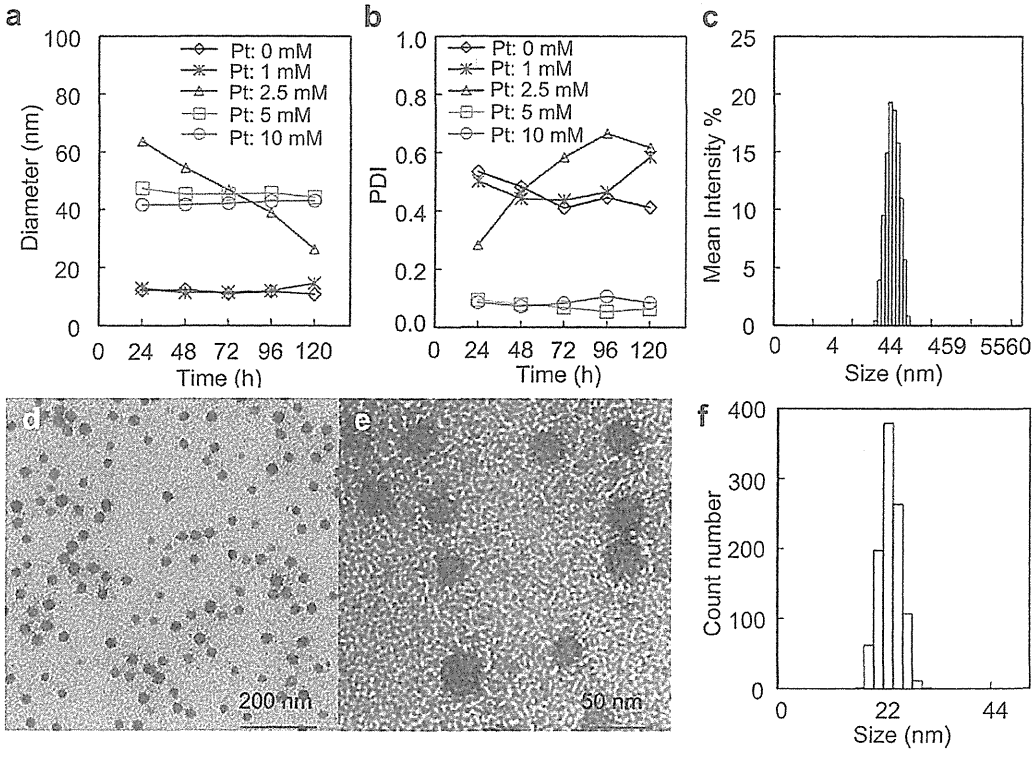

Fig. 1. Change in (a) average diameter and (b) polydispersity index (PDI) of Gd-DTPA/m with different Pt/Gd molar ratios, Gd-DTPA concentration was fixed at 5 mM, and Pt concentration ranged from 0 mM to 10 mM. (c) Size distribution measured by DLS. (d) and (e) TEM of Gd-DTPA/m. (f) Size distribution by number from TEM (n = 1012) calculated from Figure S6.

Table 1
Loading of Gd-DTPA/m prepared with different Pt/Gd ratio.

Sample (Pt:Gd-DTPA)	Pt linker loading	Gd-DTPA loading
0:5	0%	0%
1:5	~7.2%	~1.3%
2.5:5	~12.6%	~3%
5:5	~35%	~16%
10:5	~41%	~12%

Polymer PEG-*b*-PAsp (DET) 12k-45DP was used, the loading was calculated by dividing the drug amount to the total amount.

$1/T_1$ (s^{-1}) of water protons per mM concentration of CAs and calculated using expression $r_1 = (1/T_1 - 1/T_{1d})/[Gd]$, where $1/T_1$ is the longitudinal relaxation rate contrast in the presence of a paramagnetic species, $1/T_{1d}$ is the longitudinal relaxation rate contrast in the absence of a paramagnetic species and [Gd] is the concentration of paramagnetic CAs (mM). The T_1 values of Gd-DTPA, Gd-DTPA/m, or Gd-DTPA/K_2PtCl_6 solution of different Gd-DTPA/Pt ratios were measured at 37 °C in water or PBS buffer with a 0.59 T ^{1}H NMR analyzer (JNM-MU25A, JEOL) with a standard inversion-recovery pulse sequence.

2.8. Kinetic stability of Gd-DTPA/m

The stability of Gd-DTPA/m micelles under physiologic conditions was determined by DLS and static light scattering using Zetasizer Nano ZS90 (Malvern Instruments Ltd., UK). Changes of scattering light intensity were measured at defined time periods. A decrease in the scattering light intensity was associated with a decrease in the apparent molecular weight of the micelles and drug density inside the micelle core as well as in the micelle concentration. The size distribution and diameter of the Gd-DTPA/m were simultaneously monitored. The zeta-potential of Gd-DTPA/m was measured in phosphate buffer (10 mM) at pH 7.4 using Zetasizer Nano ZS90.

2.9. In vitro cytotoxicity evaluation

The cytotoxicity of Gd-DTPA/m against HUVEC and B16-F10 cell lines were evaluated by the CCK-8 assay. HUVEC and B16-F10 cells (5000 cells) were cultured with EGM-2 bullet kit and DMEM (containing 10% FBS), and then placed in 96-well plates, respectively. The cells were then exposed to Gd-DTPA, PEG-*b*-PAsp(DET), K_2PtCl_6 and Gd-DTPA/m for 72 h under 5% CO_2 at 37 °C. The Kit-8 solution was added, and followed by incubation under 5% CO_2 at 37 °C for 2.5 h. The absorbance at 450 nm of the produced WST-8 formazan in each well was measured using a using a micro-plate reader (Model 680, Bio-rad).

2.10. Cancer models

CDF_1 mice (female, 6 weeks old) were inoculated subcutaneously with C-26 cells (1×10^6 cells/mL). *In vivo* biodistribution, elemental mapping and MRI studies were performed when tumors were approximately 50 mm^3 in volume.

2.11. Biodistribution of Gd-DTPA/m

Gd-DTPA or Gd-DTPA/m was intravenously injected to the C-26 bearing mice at a dose of 78 μg/mouse on a Gd-DTPA basis. The mice were sacrificed after defined time periods (1, 4, 8 and 24 h). Tumors, livers, kidneys and spleens were excised. Blood was collected from the inferior vena cava, heparinized and centrifuged to obtain the upper plasma. Tissue samples were washed in PBS and weighed after removing excess fluid. The samples were dissolved in 90% HNO_3 and evaporated to dryness. The Pt and Gd concentrations were then measured by ICP-MS after the dried samples were dissolved in 1% HNO_3. The area under the curve (AUC) of a plot of liver, kidney, tumor and spleen drug concentration versus time was measured based on the trapezoidal rule up to 24 h after administration. Then, AUC ratios of tumor to liver, kidney and spleen are calculated.

2.12. Histology study

Mice bearing C-26 tumors were intravenously injected with Gd-DTPA/m at 100 μg/mouse on a Gd-DTPA basis. Twenty-four hours later, tumors were collected and immediately frozen in an acetone/dry ice mixture. The frozen samples were further sectioned at 6-μm thickness in a cryostat. Then, these thin sections were placed on glass slides, dehydrated in xylene and dehydrated with graded alcohols. These slides were stained with hematoxylin and eosin (H&E) and then samples were observed by using an AX80 microscope (Olympus, Japan).

2.13. In vivo MRI of Gd-DTPA/m

Solutions containing 0.2, 0.3, 0.4 and 0.5 mM Gd-DTPA or Gd-DTPA/m were placed in thin-wall PCR tubes, and then closed with flat caps for MR imaging at 1 T (Aspect, Aspect Imaging) and 7 T (BioSpec 70/20USR, Bruker). *In vivo* MR images were obtained using 1 T imaging spectrometer. For the T_1-weighted images of the mice, the following parameters were adopted: spin-echo method, repetition time (TR) = 400 ms, echo time (TE) = 11 ms, field of view (FOV) = 48 × 48 mm, matrix size = 256 × 256, and slice thickness = 2 mm. MR images were obtained from C-26 tumor bearing mice when the mean tumor volume was 100 mm^3. For all of the mice, transaxial T_1-weighted images were taken before injecting Gd-DTPA/m or Gd-DTPA as a control imaging. The mice were anesthetized with 1.8% isoflurane during the MRI experiments. The mice were injected i.v. with 0.22 mmol/kg of Gd-DTPA alone or 0.02 mmol/kg of Gd-DTPA/m based on Gd-DTPA. The transaxial T1W images were taken with a phantom containing water as a reference signal in defined time. The images were reconstructed and analyzed using ParaVision (Bruker Biospin) and Image J (NIH).

2.14. Element analysis using μ-SR-XRF

Micro-synchrotron radiation-induced X-ray fluorescence spectrometry imaging (μ-SR-XRF) was used to determine Gd-DTPA as well as Fe, Pt distribution in sections of solid tumor. Briefly, CDF_1 mice bearing C-26 tumor were intravenously injected with Gd-DTPA/m at 100 μg/mouse on a Gd-DTPA basis. Twenty-four hours later, tumors were collected and immediately frozen in acetone/dry ice, and then sliced using a cryostat and fixed on polypropylene sheets. μ-SR-XRF was performed using

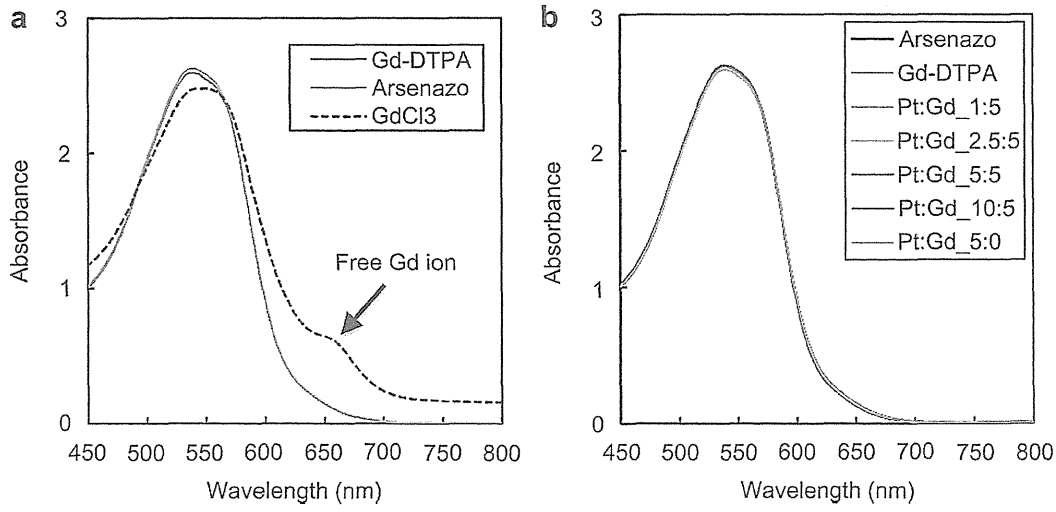

Fig. 2. Absorption spectrum of Arsenazo(III) solution with different mole ratios of Gd-DTPA and K_2PtCl_6 mixture solutions, the concentration of Gd-DTPA was maintained at 5 mM, the Pt concentration increased from 0 to 10 mM. The mixture of K_2PtCl_6 with Gd-DTPA did not compromise the stability of Gd-DTPA chelate.

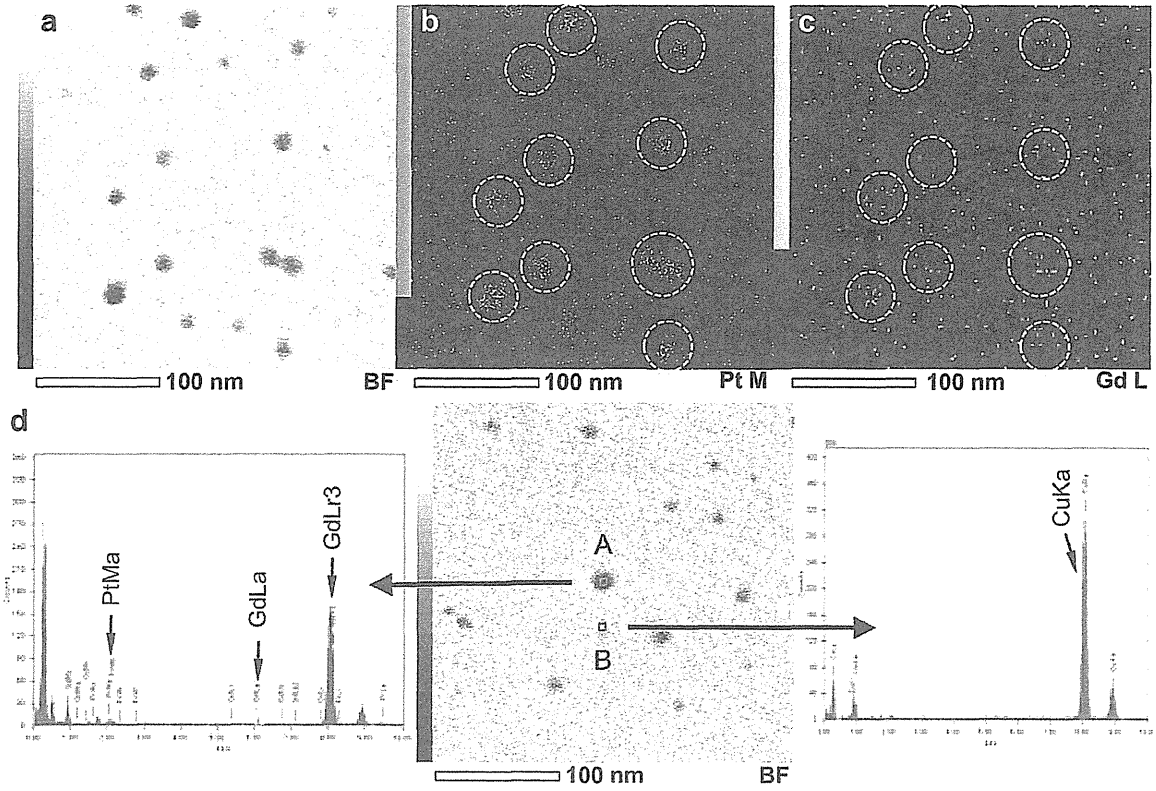

Fig. 3. EDS analysis of Gd-DTPA/m. (a) STEM image of Gd-DTPA/m. (b) Pt distribution under the STEM pattern. (c) Gd distribution under the STEM pattern. (d) EDX spectra of Gd-DTPA/m and background.

beam line 37XU at SPring-8 (Hyogo, Japan), operated at 8 GeV and ~100 mA. A photon beam with 14 keV of energy, a beam spot size of 1.3 × 1.3 μm^2, and an intensity of 1 × 10^{12} photons/s was used to irradiate the tissue sample. The fluorescence X-rays were measured using a Si-SSD in air at room temperature. Each sample on the acryl board was mounted on an x–y translation stage. The fluorescence X-ray intensity was normalized by the incident X-ray intensity, I_0, to produce a two-dimensional elemental map. An area of 250 × 250 μm^2 of the tissue sections was roughly scanned before μ-SR-XRF imaging.

3. Results and discussion

PEG-*b*-PAsp(DET) copolymers with different degree of polymerization (DP) (DP = 25, 35 and 45) were synthesized by aminolysis reaction of PEG-*b*-PBLA with diethylenetriamine (Scheme S1). PEG can hinder the interaction of the micelles with plasma proteins and prolong their circulation time in blood, while PAsp(DET) segments are minimally toxic and biodegradable as PAsp main-chain is fragmented from the nucleophilic attack of DET side chain via the formation of a succinimide ring [32]. Pt(IV) could form very stable chelates with amino groups of ethylenediamine and labile complexes with carboxylic groups [19,33]. Thus, as K_2PtCl_6 were mixed with PEG-*b*-PAsp(DET) and Gd-DTPA in aqueous solution, the block copolymers self-assembled into core–shell polymeric micelles carrying Gd-DTPA in the core as shown in Scheme 1. The K_2PtCl_6 concentration was found to be critical for the

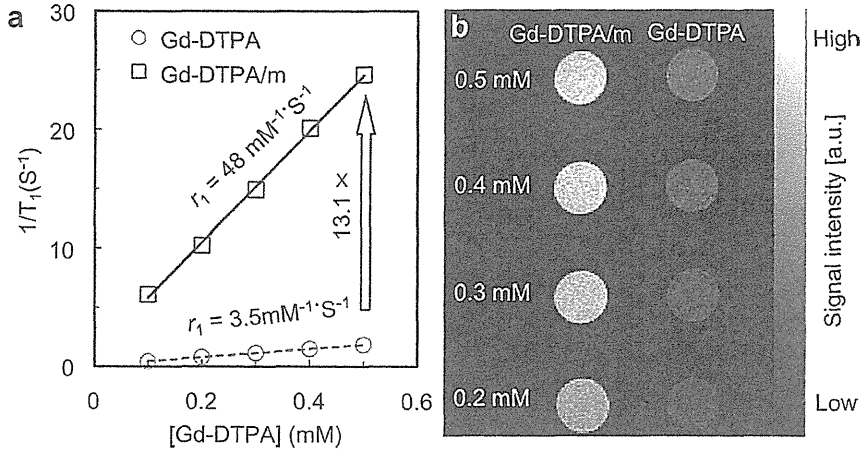

Fig. 4. MR enhancement effect of Gd-DTPA/m. (a) T_1 relaxivity coefficient. (b) T_1 weight MR images of Gd-DTPA/m and free Gd-DTPA solutions at 1 T.

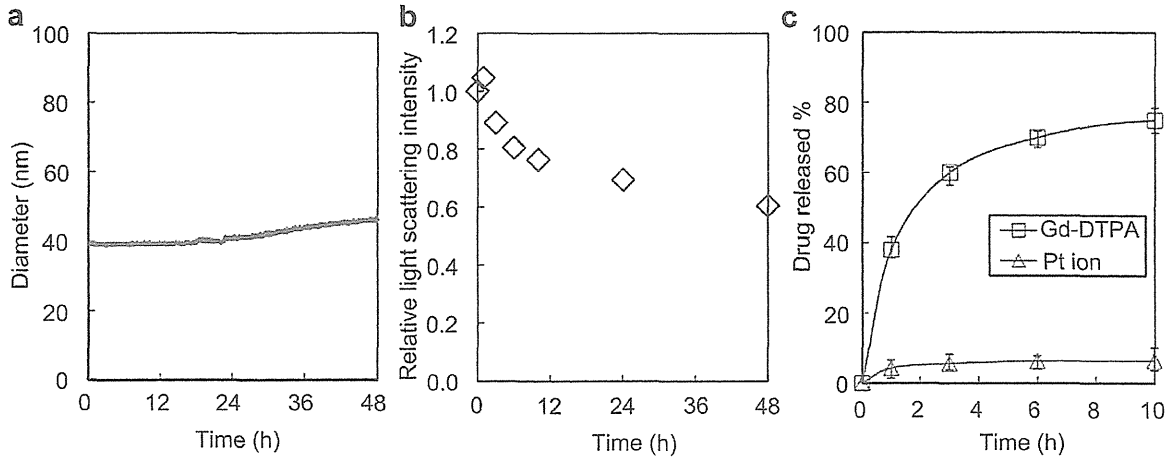

Fig. 5. Physicochemical characterization of Gd-DTPA/m under physiologic conditions. (a) Real time changes of diameter and (b) Change in relative light scattering intensity of Gd-DTPA/m. (c) Release rate of Gd-DTPA and Pt complexes from Gd-DTPA/m under similar conditions.

formation of micelles as without K_2PtCl_6, or even at low K_2PtCl_6 concentration, the micelles did not assemble (Fig. 1a and b). At 5 and 10 mM of K_2PtCl_6, narrowly distributed micelles were formed incorporating 16% and 12% of Gd-DTPA in weight, respectively (Table 1). Besides, the micelles prepared with PEG-*b*-Asp(DET) having longer PAsp(DET) segments showed higher loading of Gd-DTPA (DP = 45, 16%) than those PAsp(DET) with shorter segments (8% for DP = 25, and 9% for DP = 35) as shown in Table S1. Therefore, we decided to use Gd-DTPA/m prepared from PEG-*b*-PAsp(DET) (DP = 45), 5 mM Gd-DTPA and 5 mM K_2PtCl_6 for all of the following experiments as this composition produced micelles with highest Gd-DPTA loading. In addition, we confirmed that K_2PtCl_6 did not break the Gd-DTPA chelates as Gd^{3+} was not detectable, by arsenazo III method [31], at any ratio of Gd-DTPA/K_2PtCl_6 (Fig. 2).

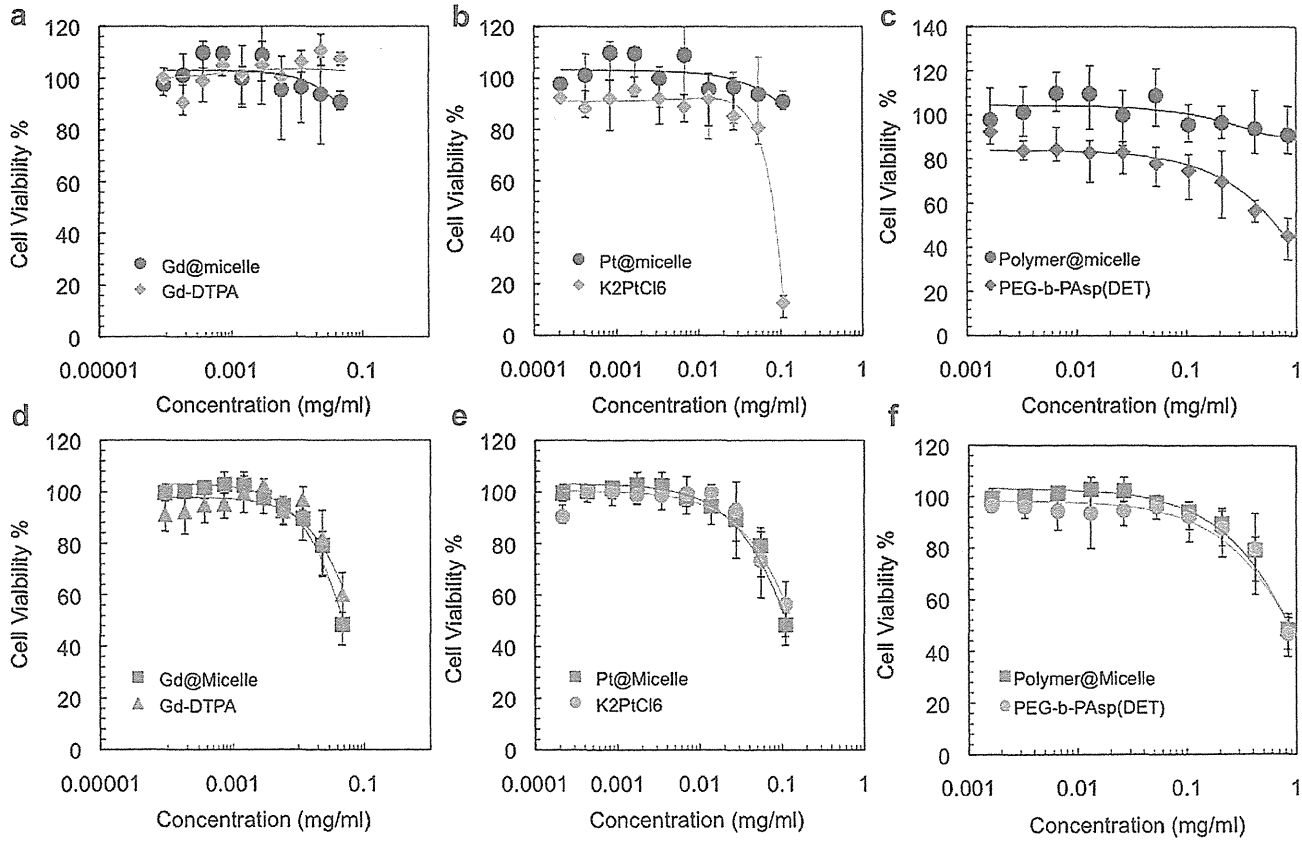

Fig. 6. Cytotoxicity of Gd-DTPA/m against HUVEC (a–c) and murine melanoma B16-F10 cells (d–f) after 72 h incubation. Micelles show comparable or even higher cell viability than free components, i.e., Gd-DTPA, K_2PtCl_6 and PEG-*b*-PAsp(DET).

The z-average diameter by intensity of these micelles was approximately 45 nm according to dynamic light scattering (Fig. 1c), and their zeta-potential was close to neutral at pH 7.4 (Figure S5). Diameter of sub-50 nm nanocarriers is important to achieve their deep tumor penetration in poorly permeable tumors according to our recent study [34]. Thus, the size of Gd-DTPA/m may be suitable for MR imaging of solid tumors with reduced permeability. According to TEM, Gd-DTPA/m showed quite narrowly distributed spherical morphology (Fig. 1d, e and Figure s6). Accordingly, the average size of the Gd-DTPA/m was calculated to be 22 nm (Fig. 1f), which is consistent with the number-averaged distribution (23 nm) calculated from z-averaged data obtained by DLS.

The elemental mapping under scanning TEM (STEM) and energy dispersive X-ray spectroscopy (EDS) of Gd-DTPA/m (Fig. 3) proved the existence of Gd and Pt elements inside the core of micelles. These results correlate with ICP-MS data (Table 1) as Pt concentration is higher than Gd encapsulated inside micelle.

The relaxivity of Gd-DTPA/m increased to 48 mM^{-1} s^{-1} based on Gd-DTPA, which is approximately 13-fold higher than that of free Gd-DTPA (Fig. 4a). T_1-weighted spin echo MRI at 1 T also revealed that Gd-DTPA/m highly improved MR contrast enhancement

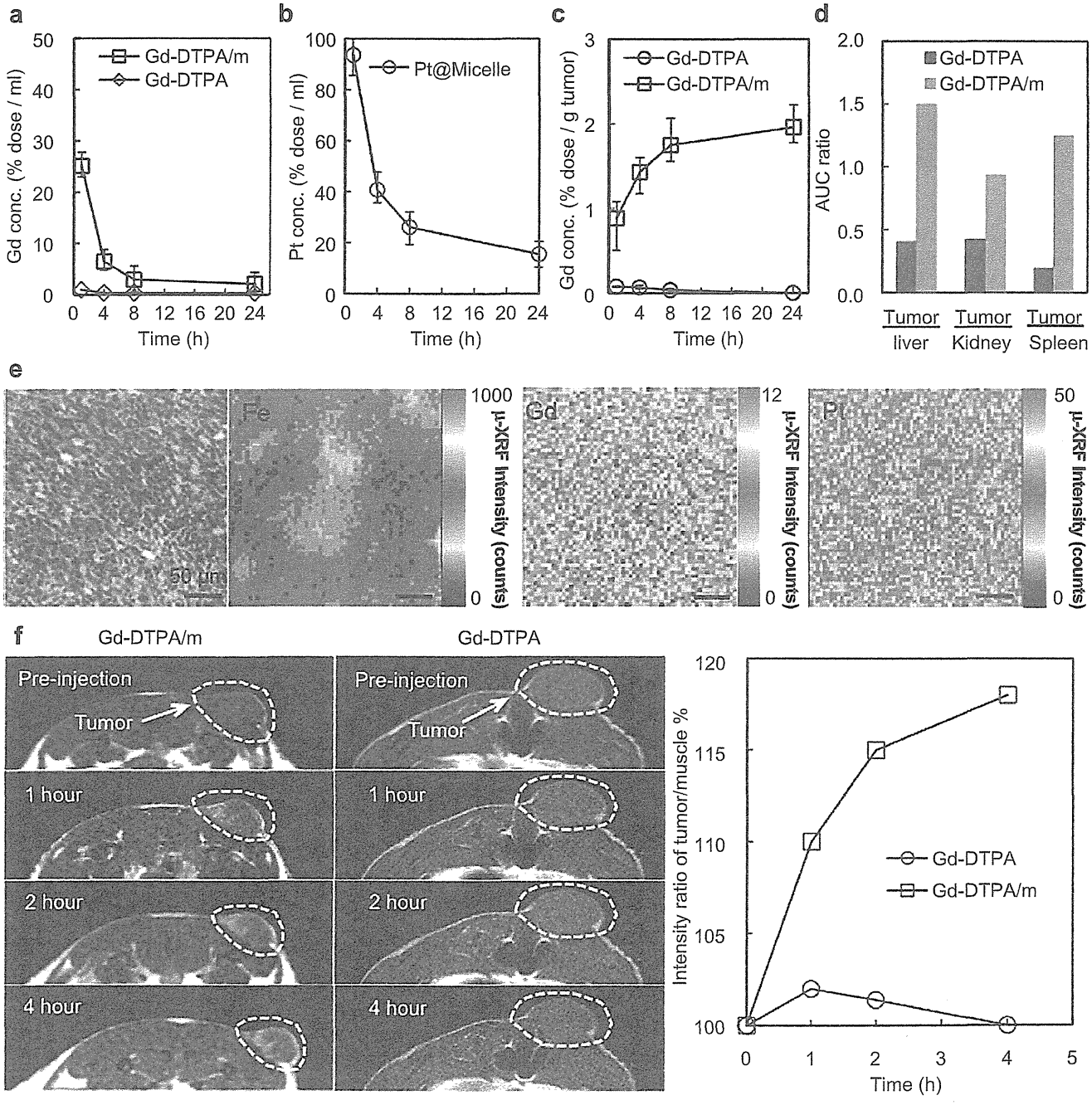

Fig. 7. *In vivo* evaluation of Gd-DTPA/m. (a) Plasma clearance of Gd-DTPA/m and free Gd-DTPA. (b) Plasma clearance of Pt@micelles. (c) Tumor accumulation of Gd-DTPA/m and free Gd-DTPA. (d) Tumor to tissue AUC ratios. (e) Microscopic findings (H&E staining) of tumor tissue and element distribution in tumor section. (f) T_1 weight tumor contrast enhancement after i.v. injection of Gd-DTPA loaded micelle and free Gd-DTPA.

compared to free Gd-DTPA (Fig. 3b), which may be attributed to a prolongation of the rotational correlation time, τ_R, due to restricted local motion similar to that of Gd-DTPA bound to macromolecules [35]. The benefits of slow rotation are observed at lower field strengths as the prevailing correlation time is almost always rotational diffusion, while at higher magnetic fields, the relaxivity of these Gd^{3+} complexes immobilized on slowly tumbling macromolecules rapidly decreases [36–38]. Accordingly, T_1-weighted spin echo MRI at 7 T showed that the contrast of Gd-DTPA/m was similar to free Gd-DTPA (Figure S7). Since clinical MRI machines use magnetic fields as high as 1.5 T, the design of Gd-DTPA/m is suitable for high relaxivity contrast enhancement at low dose. Interestingly, r_1 of Gd-DTPA/m augmented as the Pt/Gd ratio inside the core increased (Figure S8). Conversely, the r_1 relaxivity of Gd-DTPA/K_2PtCl_6 mixtures at different mole ratios or incubation time showed no significant r_1 relaxivity enhancement (Figure S9) suggesting that the incorporation of Gd-DTPA in the micelles core is necessary for the enhancement of relaxivity.

The micelles were stable under physiological conditions, i.e. in 10 mM PBS (pH 7.4) with 150 mM NaCl at 37 °C. In physiological environments, the diameter of the micelles slightly augmented after 18–20 h (Fig. 5a). Moreover, 60% of the initial light scattering intensity of the micelles was detectable even after 48 h (Fig. 5b). During the exposure of the micelles to physiological conditions, 75% Gd-DTPA was released in approximately 10 h, while only 7% of Pt was released probably due to stable metal complexation of Pt(IV) with PEG-*b*-PAsp(DET) (Fig. 5c). The ability of Gd-DTPA/m to sustainedly release Gd-DTPA, which can undergo glomerular filtration in the kidneys, may reduce the risk of free Gd discharge in the body.

Gd-DTPA/m was not cytotoxic against both primary cell lines (HUVEC) and tumor cell lines (B16-F10) (Fig. 6), suggesting its safety for *in vivo* application. Gd-DTPA/m extended the circulation of Gd-DTPA in the bloodstream, attaining 5% of the injected dose of Gd-DTPA after 8 h, while free Gd-DTPA was rapidly cleared from plasma (Fig. 7a and b). Moreover, approximately 15% of the injected Pt remained in the bloodstream after 24 h, which indicates the circulation of the micelles in the bloodstream. Gd-DTPA/m was able to deliver 26-fold higher CA in subcutaneous murine colon adenocarcinoma 26 (C-26) than free Gd-DTPA (Fig. 7c). In addition, the ratio of AUC in tumor versus organs indicated that Gd-DTPA/m improved the tumor-to-organ distribution of Gd-DTPA (Fig. 7d).

The microdistribution of the drugs at the tumor site was studied by micro-synchrotron radiation-induced X-ray fluorescence spectrometry imaging (μ-SR-XRF) of the tumor sites as Pt and Gd showed very distinct peaks in the sum spectrum of the line scan. Moreover, Fe mapping was also evaluated as it characterizes hemeproteins and therefore the positioning of blood vessels in the tissue. The atoms of Gd as well as Pt located in the whole tumor section in areas far from the Fe-rich regions suggesting deep tumor penetration and accumulation of Gd-DTPA/m as shown in Fig. 7e, in which the rainbow scales represent the quantity of element.

The size, neutral surface charge, stability and release characteristics of Gd-DTPA/m may contribute to the high penetration and accumulation of Gd-DTPA at the tumor site. The higher tumor accumulation and higher relaxivity of Gd-DTPA/m clearly and selectively enhanced the contrast at the tumor area in T_1-weighted MR images, even at low dose (0.02 mmol/kg based on Gd-DTPA) of contrast agents (Fig. 7f). The tumor selective contrast enhancement of Gd-DTPA/m was significant from 1 h after injection until the end of the experiment, that is, 4 h after injection. Oppositely, intravenously injected free Gd-DTPA, even at a 10 times higher dose, that is, 0.22 mmol/kg, failed to increase the intensity of the signal in the tumor region. These findings indicate the potential of GD-DTPA/m as a tumor-selective contrast agent.

4. Conclusion

Gd-DTPA/m efficiently improved the MRI-contrast of solid tumors demonstrating its potential application in the bio-imaging field. Accordingly, the sub-50 nm size, neutral surface and biological stability of Gd-DTPA/m, and the increased relaxivity of Gd-DTPA in the core of micelles lead to selective contrast enhancement of tumors. This facile and reversible metal complexation used for the construction of Gd-DTPA/m could also be applied for incorporating hydrophilic imaging probes, therapeutic drugs, or bioactive molecules into nanodevices for diagnosis and therapy. Accordingly, here, we illustrated a new approach for designing nano-sized vehicles by incorporating drugs via metal complexation besides widely used methods, such as covalent conjugation, or hydrophobic interaction, demonstrating its further application for loading compounds, which are difficult to incorporate in traditional nanocarriers.

Acknowledgments

This work was financially supported by the Japan Society for the Promotion of Science (JSPS) through its "Funding Program for World-Leading Innovative R&D on Science and Technology (FIRST Program)". TEM experiments were conducted in Research Hub for Advanced Nano Characterization, The University of Tokyo, supported by the Ministry of Education, Culture, Sports, Science and Technology (MEXT), Japan. P. M. acknowledges the fellowship from Ministry of Education, Science, Sports and Culture (MEXT), Japan. The authors are grateful Mr. Hashime Hoshi (JEOL), Ms. Sayaka Shibata and Aiko Sekita (NIRS) for technical support.

Appendix A. Supplementary data

Supplementary data related to this article can be found at http://dx.doi.org/10.1016/j.biomaterials.2012.09.030.

References

[1] Weissleder R, Pittet MJ. Imaging in the era of molecular oncology. Nature 2008;452:580–9.
[2] Mansfield P. Snapshot magnetic resonance imaging. Angew Chem Int Ed 2004; 43:5456–64.
[3] Weinmann HJ, Brasch RC, Press WR, Wesbey GE. Characteristics of gadolinium-DTPA complex: a potential NMR contrast agent. AJR Am J Roentgenol 1984; 142:619–24.
[4] Davis PL, Kaufman L, Crooks LE, Miller TR. Detectability of hepatomas in rat livers by nuclear magnetic resonance imaging. Invest Radiol 1981;16:354–9.
[5] Laurent S, Elst LV, Muller RN. Comparative study of the physicochemical properties of six clinical low molecular weight gadolinium contrast agents. Contrast Media Mol Imaging 2006;1:128–37.
[6] Ananta JS, Godin B, Sethi R, Moriggi L, Liu XW, Serda RE, et al. Geometrical confinement of gadolinium-based contrast agents in nanoporous particles enhances T-1 contrast. Nat Nanotech 2010;5:815–21.
[7] Thompson KH, Orvig C. Boon and bane of metal ions in medicine. Science 2003;300:936–9.
[8] Ferrari M. Cancer nanotechnology: opportunities and challenges. Nat Rev Cancer 2005;5:161–71.
[9] Cabral H, Nishiyama N, Kataoka K. Supramolecular nanodevices: from design validation to theranostic nanomedicine. Acc Chem Res 2011;44:999–1008.
[10] Kataoka K, Harada A, Nagasaki Y. Block copolymer micelles for drug delivery: design, characterization and biological significance. Adv Drug Deliv Rev 2001; 47:113–31.
[11] Nishiyama N, Morimoto Y, Jang WD, Kataoka K. Design and development of dendrimer photosensitizer-incorporated polymeric micelles for enhanced photodynamic therapy. Adv Drug Deliv Rev 2009;61:327–38.
[12] Rafi M, Cabral H, Kano MR, Mi P, Iwata C, Yashiro M, et al. Polymeric micelles incorporating (1,2-diaminocyclohexane)platinum (II) suppress the growth of orthotopic scirrhous gastric tumors and their lymph node metastasis. J Control Release 2012;159:189–96.
[13] Mikhaylov G, Mikac U, Magaeva AA, Itin VI, Naiden EP, Psakhye I, et al. Ferri-liposomes as an MRI-visible drug-delivery system for targeting tumours and their microenvironment. Nat Nanotech 2011;6:594–602.

[14] Floyd III WC, Klemm PJ, Smiles DE, Kohlgruber AC, Pierre VC, Mynar JL, et al. Conjugation effects of various linkers on Gd(III) MRI contrast agents with dendrimers: optimizing the hydroxypyridinonate (HOPO) ligands with nontoxic, degradable esteramide (EA) dendrimers for high relaxivity. J Am Chem Soc 2011;133:2390–3.
[15] Kojima C, Turkbey B, Ogawa M, Bernardo M, Regino CAS, Bryant LH, et al. Dendrimer-based MRI contrast agents: the effects of PEGylation on relaxivity and pharmacokinetics. Nanomedicine 2011;7:1001–8.
[16] Khemtong C, Kessinger CW, Ren J, Bey EA, Yang SG, Guthi JS, et al. In vivo off-resonance saturation magnetic resonance imaging of alphavbeta3-targeted superparamagnetic nanoparticles. Cancer Res 2009;69:1651–8.
[17] Mulder WJM, Strijkers GJ, van Tilborg GAF, Griffioen AW, Nicolay K. Lipid-based nanoparticles for contrast-enhanced MRI and molecular imaging. NMR Biomed 2006;19:142–64.
[18] Ai H. Layer-by-layer capsules for magnetic resonance imaging and drug delivery. Adv Drug Deliv Rev 2011;63:772–88.
[19] Vucic E, Sanders HM, Arena F, Terreno E, Aime S, Nicolay K, et al. Well-defined, multifunctional nanostructures of a paramagnetic lipid and a lipopeptide for macrophage imaging. J Am Chem Soc 2009;131:406–7.
[20] Kaida S, Cabral H, Kumagai M, Kishimura A, Terada Y, Sekino M, et al. Visible drug delivery by supramolecular nanocarriers directing to single-platformed diagnosis and therapy of pancreatic tumor model. Cancer Res 2010;70:7031–41.
[21] Nasongkla N, Bey E, Ren JM, Ai H, Khemtong C, Guthi JS, et al. Multifunctional polymeric micelles as cancer-targeted, MRI-ultrasensitive drug delivery systems. Nano Lett 2006;6:2427–30.
[22] Yokoyama M, Nakamura E, Makino K, Okano T, Yamamoto TA. Polymeric micelle MRI contrast agent with changeable relaxivity. J Control Release 2006; 114:325–33.
[23] Manus LM, Mastarone DJ, Waters EA, Zhang XQ, Schultz-Sikma EA, MacRenaris KW, et al. Gd(III)-nanodiamond conjugates for MRI contrast enhancement. Nano Lett 2010;10:484–9.
[24] Torchilin VP. PEG-based micelles as carriers of contrast agents for different imaging modalities. Adv Drug Deliv Rev 2002;54:235–52.
[25] Ai H, Flask C, Weinberg B, Shuai X, Pagel MD, Farrell D, et al. Magnetite-loaded polymeric micelles as ultrasensitive magnetic-resonance probes. Adv Mater 2005;17:1949–52.
[26] Duncan R, Izzo L. Dendrimer biocompatibility and toxicity. Adv Drug Deliv Rev 2005;57:2215–37.
[27] Matsumura Y, Kataoka K. Preclinical and clinical studies of anticancer agent-incorporating polymer micelles. Cancer Sci 2009;100:572–9.
[28] Plummer R, Wilson RH, Calvert H, Boddy AV, Griffin M, Sludden J, et al. A phase I clinical study of cisplatin-incorporated polymeric micelles (NC-6004) in patients with solid tumours. Br J Cancer 2011;104:593–8.
[29] Harada A, Kataoka K. Formation of polyion complex micelles in an aqueous milieu from a pair of oppositely-charged block-copolymers with poly(ethylene glycol) segments. Macromolecules 1995;28:5294–9.
[30] Kanayama N, Fukushima S, Nishiyama N, Itaka K, Jang WD, Miyata K, et al. A PEG-based biocompatible block catiomer with high buffering capacity for the construction of polyplex micelles showing efficient gene transfer toward primary cells. ChemMedChem 2006;1:439–44.
[31] Gouin S, Winnik FM. Quantitative assays of the amount of diethylene-triaminepentaacetic acid conjugated to water-soluble polymers using isothermal titration calorimetry and colorimetry. Bioconjug Chem 2001;12: 372–7.
[32] Itaka K, Ishii T, Hasegawa Y, Kataoka K. Biodegradable polyamino acid-based polycations as safe and effective gene carrier minimizing cumulative toxicity. Biomaterials 2010;31:3707–14.
[33] Iakovidis A, Hadjiliadis N. Complex-compounds of platinum(II) and platinum(IV) with amino-acids, peptides and their derivatives. Coord Chem Rev 1994;135:17–63.
[34] Cabral H, Matsumoto Y, Mizuno K, Chen Q, Murakami M, Kimura M, et al. Accumulation of sub-100nm polymeric micelles in poorly permeable tumours depends on size. Nat Nanotech 2011;6:815–23.
[35] Caravan P, Ellison JJ, McMurry TJ, Lauffer RB. Gadolinium(III) chelates as MRI contrast agents: structure, dynamics, and applications. Chem Rev 1999;99: 2293–352.
[36] Terreno E, Castelli DD, Viale A, Aime S. Challenges for molecular magnetic resonance imaging. Chem Rev 2010;110:3019–42.
[37] Mastarone DJ, Harrison VSR, Eckermann AL, Parigi G, Luchinat C, Meade TJ. A modular system for the synthesis of multiplexed magnetic resonance probes. J Am Chem Soc 2011;133:5329–37.
[38] Caravan P, Farrar CT, Frullano L, Uppal R. Influence of molecular parameters and increasing magnetic field strength on relaxivity of gadolinium- and manganese-based T1 contrast agents. Contrast Media Mol Imaging 2009;4: 89–100.

Cell Stem Cell
Short Article

Generation of Rejuvenated Antigen-Specific T Cells by Reprogramming to Pluripotency and Redifferentiation

Toshinobu Nishimura,[1] Shin Kaneko,[1,9,*] Ai Kawana-Tachikawa,[2] Yoko Tajima,[1] Haruo Goto,[1] Dayong Zhu,[2] Kaori Nakayama-Hosoya,[2] Shoichi Iriguchi,[1] Yasushi Uemura,[6] Takafumi Shimizu,[1] Naoya Takayama,[3,10] Daisuke Yamada,[7] Ken Nishimura,[8] Manami Ohtaka,[8] Nobukazu Watanabe,[4] Satoshi Takahashi,[5] Aikichi Iwamoto,[2] Haruhiko Koseki,[7] Mahito Nakanishi,[8] Koji Eto,[3,10] and Hiromitsu Nakauchi[1,*]

[1]Division of Stem Cell Therapy, Center for Stem Cell Biology and Regenerative Medicine
[2]Division of Infectious Diseases, Advanced Clinical Research Center
[3]Stem Cell Bank, Center for Stem Cell Biology and Regenerative Medicine
[4]Laboratory of Diagnostic Medicine, Center for Stem Cell Biology and Regenerative Medicine
[5]Division of Molecular Therapy, Advanced Clinical Research Center
The Institute of Medical Science, The University of Tokyo, 4-6-1 Shirokanedai, Minato-ku, Tokyo 108-8639, Japan
[6]Division of Immunology, Aichi Cancer Center Research Institute, 1-1 Kanakoden, Chikusa-ku Nagoya, Aichi 464-8681, Japan
[7]Laboratory for Lymphocyte Development, RIKEN Center for Allergy and Immunology, 1-7-22 Suehiro-cho, Tsurumi-ku, Yokohama, Kanagawa 230-0045, Japan
[8]Research Center for Stem Cell Engineering, National Institute of Advanced Industrial Science and Technology, 1-1-1 Higashi, Central 4, Tsukuba, Ibaraki 305-8562, Japan
[9]Present address: Department of Fundamental Cell Technology, Center for iPS Cell Research and Application (CiRA), Kyoto University, 53 Kawahara-cho, Shogoin, Sakyo-ku, Kyoto 606-8507, Japan
[10]Present address: Department of Clinical Application, CiRA, Kyoto University, 53 Kawahara-cho, Shogoin, Sakyo-ku, Kyoto 606-8507, Japan
*Correspondence: kaneko.shin@cira.kyoto-u.ac.jp (S.K.), nakauchi@ims.u-tokyo.ac.jp (H.N.)
http://dx.doi.org/10.1016/j.stem.2012.11.002

SUMMARY

Adoptive immunotherapy with functional T cells is potentially an effective therapeutic strategy for combating many types of cancer and viral infection. However, exhaustion of antigen-specific T cells represents a major challenge to this type of approach. In an effort to overcome this problem, we reprogrammed clonally expanded antigen-specific CD8$^+$ T cells from an HIV-1-infected patient to pluripotency. The T cell-derived induced pluripotent stem cells were then redifferentiated into CD8$^+$ T cells that had a high proliferative capacity and elongated telomeres. These "rejuvenated" cells possessed antigen-specific killing activity and exhibited T cell receptor gene-rearrangement patterns identical to those of the original T cell clone from the patient. We also found that this method can be effective for generating specific T cells for other pathology-associated antigens. Thus, this type of approach may have broad applications in the field of adoptive immunotherapy.

INTRODUCTION

T cells play a central role in acquired immunity and the configuration of systemic immunity against pathogens. In particular, cytotoxic T lymphocytes (CTLs) are major components of this systemic response to microorganisms, viral infections, and neoplasms (Greenberg, 1991; Zhang and Bevan, 2011). T cells initiate their proliferative and effector functions upon human leukocyte antigen (HLA)-restricted recognition of specific antigen peptides via T cell receptors (TCRs). This is greatly beneficial in enabling the selective recognition and eradication of target cells, and also in long-term immunological surveillance by long-lived memory T cells (Butler et al., 2011; Jameson and Masopust, 2009; MacLeod et al., 2010). However, viruses in chronic infection or cancers often hamper or escape the T cell immunity by decreasing the expression of molecules required for T cell recognition or by inhibiting antigen presentation (Virgin et al., 2009). In addition, continuous exposure to chronically expressed viral antigens or cancer/self-antigens can drive T cells into an "exhausted" state. This is characterized by loss of effector functions and the potential for long-term survival and proliferation, ultimately leading to the depletion of antigen-responding T cell pools (Klebanoff et al., 2006; Wherry, 2011).

The infusion of ex vivo-expanded autologous antigen-specific T cells is being developed clinically for T cell immunotherapy. However, up to now, highly expanded T cells have not proven to be particularly effective (June, 2007). This is in part explained by losses of function that occur during the ex vivo manipulation of patient autologous T cells. In another instance, genetic modification of antigen receptors is an ambitious but only partially successful way to add desired antigen specificity to nonspecific T cells (Morgan et al., 2006; Porter et al., 2011). The therapeutic effect also strongly depends on the extent of functional loss that occurs during the ex vivo manipulation of T cells and on the stability of exogenous antigen receptor expression specific to target molecules in the presence of the endogenous TCR genes (Bendle et al., 2010; Brenner and Okur, 2009).

For the purpose of overcoming these obstacles, the therapeutic potential of induced pluripotent stem cells (iPSCs) is being

explored. Embryonic stem cells (ESCs) or iPSCs have the capacity for self-renewal while maintaining pluripotency (Takahashi et al., 2007) and could potentially form the basis for the unlimited induction of antigen-specific juvenile T cells. However, there are challenges to this approach as well, given that methods for the differentiation and immunological education of ESCs and iPSCs, or indeed that of intermediate hematopoietic stem and/or progenitor cells, into fully matured functional human T cells are not well established (Timmermans et al., 2009). Reprogramming the nuclei of lymphocytes was historically performed for studying whether terminally differentiated or fully matured somatic cells could revert to a pluripotent state. The first demonstration of lymphocyte reprogramming employed somatic cell nuclear transfer in murine B and T cells, proving that terminally differentiated somatic cells were reprogrammable (Hochedlinger and Jaenisch, 2002). Reprogramming murine B cells into pluripotent stem cells by iPSC technology also provided definite proof for fate reversibility in fully matured somatic cells (Hanna et al., 2008). From another point of view, nuclear reprogramming of lymphocytes is seen as having applications for regenerative medicine different than those for scientific research. The irreversible rearrangement of genes encoding immunoglobulins and TCRs was recognized solely as a genetic marker in somatic cell nuclear transfer and iPSC research. However, the preserved rearrangements in genomic DNA can also provide a blueprint of "educated" weapons for attacking cancers and pathogens in adoptive immunotherapy. Although several groups have reported the generation of T cell-derived iPSCs (T-iPSCs), their clinical applications have yet to be thoroughly explored (Brown et al., 2010; Loh et al., 2010; Seki et al., 2010; Staerk et al., 2010).

In the present study, we chose a T cell clone specific to an HIV type 1 (HIV-1) epitope of known structure to act as a generic representation of iPSC-mediated T cell regeneration. We successfully induced iPSCs from antigen-specific T cells and redifferentiated them into functional T cells. This may act as proof of concept for the application of "rejuvenated" T cells in treating various diseases. Crucial to this concept was that T-iPSCs retained the assembled "endogenous" TCR genes even after being subjected to nuclear reprogramming. Furthermore, redifferentiated T cells showed the same pattern of TCR gene arrangement as that in the original T cells. These features may therefore serve as the foundation for the reproduction of unlimited numbers of T cells that express desired TCRs conferring to antigen specificity.

RESULTS

Reprogramming an Antigen-Specific Cytotoxic T Cell Clone into Pluripotency

To establish T cell-derived iPSCs, we magnetically separated the $CD3^+$ T cell population from peripheral blood mononuclear cells (PBMCs) of healthy volunteers. The isolated $CD3^+$ T cells were stimulated with human CD3 and CD28 antibody-coated microbeads (α-CD3/28 beads) in the presence of interleukin-2 (IL-2). We then transduced the activated $CD3^+$ T cells with separate retroviral vectors that individually code for *OCT3/4*, *SOX2*, *KLF4*, and c-*MYC*. Human ESC-like colonies were obtained within 25 days of culture (Figure S1A available online).

We also isolated PBMCs from an HLA-A24-positive patient with a chronic HIV-1 infection. $CD8^+$ CTL clones specific for an antigenic peptide (amino acids [aa] 138–145) from the HIV-1 Nef protein (Nef-138-8(WT); RYPLTFGW) (Altfeld et al., 2006) were established. One of the clones, H25-#4, was stimulated using α-CD3/28 beads in the presence of IL-2 and then transduced simultaneously with six retroviral vectors encoding *OCT3/4*, *SOX2*, *KLF4*, c-*MYC*, *NANOG*, and *LIN28A*. However, we could not reprogram H25-#4 into pluripotency, possibly due to the cells being in a low infectious and exhausted state, or due to insufficient expression of the reprogramming factors. In response, we attempted to increase transduction efficiency and transgene expression by using two Sendai virus (SeV) vectors. One of them encodes tetracistronic factors (*OCT3/4*, *SOX2*, *KLF4*, and c-*MYC*) (Nishimura et al., 2011) with the miR-302 target sequence (SeVp[KOSM302L]; K.N., M.O., and M.N., data not shown), and another encodes SV40 large T antigen (SeV18[T]) (Fusaki et al., 2009). After transduction of phytohemagglutinin (PHA)-activated H25-#4 cells with the SeV vectors in the presence of IL-7 and IL-15, sufficient numbers of human ESC-like colonies appeared within 40 days of culture (Figure 1A). Use of this SeV system and optimization of transduction conditions greatly improved the reprogramming efficiency. It enabled us to reprogram several $CD8^+$ or $CD4^+$ T cell clones specific to pp65 antigen in cytomegalovirus (CMV), glutamic acid decarboxylase (GAD) antigen in type 1 diabetes, and α-GalCer (Table 1).

The resultant $CD3^+$ T cell- and H25-#4-derived ESC-like colonies (TkT3V1-7 and H254SeVT-3, respectively) exhibited alkaline phosphatase (AP) activity and expressed the pluripotent cell markers SSEA-4, Tra-1-60, and Tra-1-81 (Figures S1B–S1E and 1B–1E). H254SeVT-3 expressed HLA-A24 (Figure 1F). Both TkT3V1-7 and H254SeVT-3 also expressed human ESC-related genes (Figures S1F and 1G). The expression of exogenous reprogramming factors from the integrated provirus (TkT3V1-7) was halted (Figure S1F), and nonintegrated SeV genomic RNA was successfully removed from the cytosol by RNAi or by self-degradation caused by temperature-sensitive mutations (H254SeVT-3) (Figure 1H). Comparison of gene-expression profiles revealed that the gene-expression patterns in the ESC-like cells were similar to those in human ESCs, but differed significantly from those in peripheral blood (PB) T cells (Figure S1G). Scant methylation of the *OCT3/4* and *NANOG* promoter regions was confirmed using bisulfite PCR, thus indicating successful reprogramming (Freberg et al., 2007) (Figures S1H and 1I). In addition, when injected into nonobese diabetic severe combined immunodeficient (NOD-Scid) mice, those cells formed teratomas containing characteristic tissues derived from all three germ layers, which is indicative of pluripotency (Brivanlou et al., 2003) (Figures S3 and 2A). Therefore, those colonies were confirmed as typical human iPSCs.

T-iPSCs Carry Preassembled TCR Genes from the Original T Cell

Almost all TCRs are composed of heterodimerically associated α and β chains. *TCRA* or *TCRB* gene (encoding α chain or β chain, respectively) rearrangements are involved in normal αβ T cell development in the thymus. These rearrangements enabled us to determine retrospectively whether the iPSCs were derived from an αβ T cell. The BIOMED-2 consortium designed multiplex-PCR primers for analyzing *TCRB* gene assemblies (van Dongen et al., 2003), and we designed the primers for detecting *TCRA*

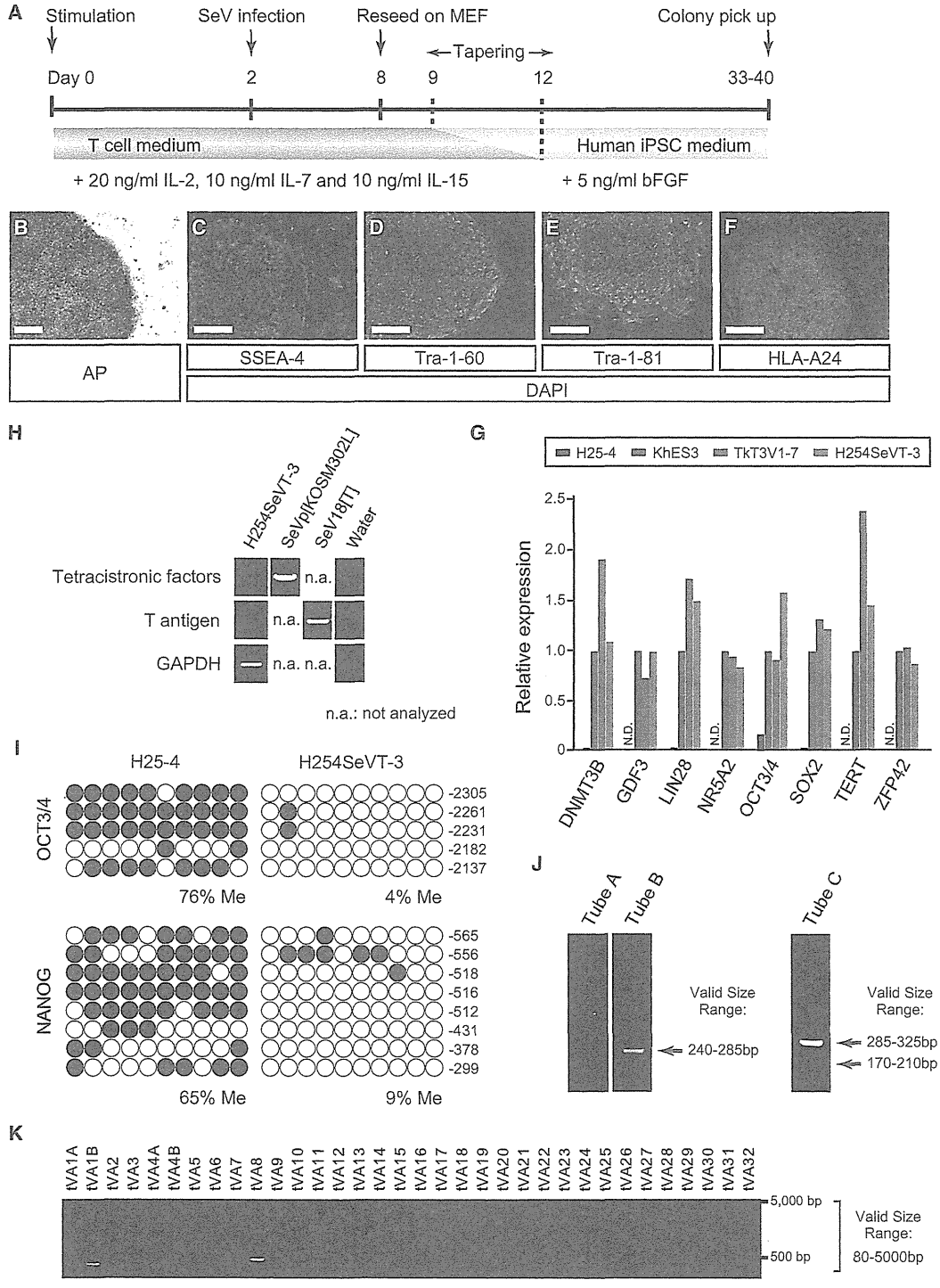

Figure 1. Generation of Human iPSCs from a CTL Clone

(A) Schematic illustration showing the generation of T-iPSCs from H25-#4 T cells using SeV vectors encoding polycistronic *OCT3/4*, *SOX2*, *KLF4*, and c-*MYC*, or SV40 large T antigen. The "tapering" indicates the gradual replacement of culture medium with human iPSC medium.

(B–F) AP activity (B) and expression of pluripotency markers (SSEA-4, C; Tra-1-60, D; and Tra-1-81, E) and HLA-A24 (F) in H254SeVT-3 cells. Nuclei were counterstained with DAPI. The scale bar represents 200 μm.

(G) Quantitative PCR for pluripotency genes in H25-#4, KhES3, TkT3V1-7, and H254SeVT-3 cells. Individual PCR reactions were normalized against 18S ribosomal RNA (rRNA).

(legend continued on next page)

Table 1. Generation of Human T-iPSCs from Various Patient-Derived T Cell Specimens

Antigen	T Cell Source	Initial Cell Number	No. of ESC-like Colonies	No. of Colonies Picked up for Establishing T-iPSC Clones	Date (MM/YYYY)
HIV-1 Nef	monoclonal T cell clone	4×10^5	7	7	05/2011
CMV pp65	polyclonal tetramer-sorted cells	~5,000	15	15	07/2011
GAD	monoclonal T cell clone	1×10^6	>100	not picked up	08/2012
		5×10^5	>100	19	08/2012
α-GalCer	FACS-sorted Vα24$^+$ cells	1×10^6	>100	not picked up	08/2012
		5×10^5	>100	7	08/2012

Sample cells were transduced with *OCT3/4*, *SOX2*, *KLF4*, *c-MYC*, and SV40 large T-antigen by using two Sendai virus (SeV) vectors (SeVp [KOSM302L] and SeV18[T]). After around 40 days, the number of embryonic stem cell (ESC)-like colonies were counted on the basis of morphology and alkaline phosphatase (AP) activity. All established T cell-derived induced pluripotent stem cell (T-iPSC) lines were free from residual SeV vectors (one example in the case of the HIV-1 Nef-specific T-iPSC clone is shown in Figure 1H). CMV, cytomegalovirus; GAD, glutamic acid decarboxylase; FACS, fluorescence-activated cell sorting.

gene assemblies (Figure S2). *TCRB* and *TCRA* gene assemblies were identified as single bands representing each allele in TkT3V1-7 and H254SeVT-3 (Figures S1H, S1I, 1J, and 1K).

We next confirmed the presence of an antigen-recognition site on the TCR that consisted of three complementarity-determining regions (CDR1, CDR2, and CDR3). CDR3 is the most diversifiable among the three because it spans the V(D)J-junction region, where several random nucleotides (N or P nucleotides) are inserted (Alt and Baltimore, 1982; Lafaille et al., 1989). We determined the CDR3 sequences of the assembled *TCRA* and *TCRB* genes in TkT3V1-7 and H254SeVT-3 and identified a set of productive *TCRA* and *TCRB* gene rearrangements (i.e., in-frame junction with no stop codon) (Table S1 and Table 2). Furthermore, the sequences of CDR3 from H254SeVT-3 and H25-#4 were completely identical at both *TCRA* and *TCRB* gene loci. These results indicated that the iPSCs established were derived from a single T cell and that the antigen specificity encoded in the genomic DNA of the T cell was conserved during reprogramming.

Redifferentiation of T-iPSCs into CD8 Single-Positive T Cells Expressing the Desired TCR

Following the application of specific in vitro differentiation protocols, iPSCs can give rise to mesoderm-derived cell types, especially hematopoietic stem and/or progenitor cells (Takayama et al., 2008; Vodyanik et al., 2005) (Figure 2B). This was applied to assess the capacity of T-iPSCs for hematopoietic differentiation by coculturing on C3H10T1/2 feeder cells in the presence of VEGF, SCF, and FLT-3L for the generation of CD34$^+$ hematopoietic stem and/or progenitor cells. On day 14 of culture, the cells were transferred onto Delta-like 1-expressing OP9 (OP9-DL1) feeder cells (Timmermans et al., 2009) and were cocultured in the presence of FLT-3L and IL-7 (Ikawa et al., 2010) (Figure 2B). After 21–28 days of culture, the hematopoietic cells differentiated into CD45$^+$, CD38$^+$, CD7$^+$, CD45RA$^+$, CD3$^+$, and TCRαβ$^+$ T lineage cells (Figure S4). As was the case with TCRαβ transgenic mice (Borgulya et al., 1992) and chimeric mice derived from ESCs produced through nuclear transplantation of T cells (Serwold et al., 2007), aberrant expression of TCRαβ was observed at the CD4/CD8 double-negative (DN) stage. Although some of these T lineage cells differentiated into the CD4/CD8 double-positive (DP) stage and the more mature CD4 or CD8 single-positive (SP) stages (Figure 2C), we could not characterize the small number of SP cells in more detail.

During thymocyte development, the CD4/CD8 DN and DP stages correspond respectively to the *TCRB*-encoded β chain and *TCRA*-encoded α chain assembly stages (von Boehmer, 2004). In the *TCRB* locus, the negative-feedback regulation of gene assembly and the capacity to deter further rearrangement are very strict (Khor and Sleckman, 2002). In the *TCRA* locus, by contrast, negative-feedback regulation is relatively loose, and further gene assembly of the preassembled gene, a phenomenon known as "receptor revision," tends to occur (Huang and Kanagawa, 2001; Krangel, 2009). In experiments using TCRα transgenic mice, the reactivation of *Rag1* and *Rag2*, genes related to recombination machinery, occurred in CD4/CD8 DP-stage thymocytes, and gene assembly of endogenous *Tcra* was observed (Padovan et al., 1993; Petrie et al., 1993). Such further gene assembly would be exceedingly undesirable for our purposes, because it would probably convert the tropism of the TCR and render the redifferentiated T cells incapable of attacking the previously targeted antigen. To determine whether such receptor revision could occur in redifferentiating T lineage cells, we collected CD1a$^-$ DN- and CD1a$^+$ DP-stage cells from among the CD45$^+$, CD3$^+$, TCRαβ$^+$, and CD5$^+$ T lineage cells and then analyzed the gene rearrangement of TCR messenger RNAs (mRNAs) (Figures S5A–S5C). Nucleotide sequences of *TCRB* mRNAs in the T lineage cells were identical to those in

(H) Detection of the remnants of SeV genomic RNAs by RT-PCR. Each column represents the template cDNA synthesized from H254SeVT-3 cells, SeVp [KOSM302L] virus solution, and SeV18[T] virus solution. cDNAs from virus solution were the positive controls.
(I) Bisulfite sequencing analyses of the *OCT3/4* and *NANOG* promoter regions in H25-#4 and H254SeVT-3 cells. White and black circles represent unmethylated and methylated (Me) CpG dinucleotides, respectively.
(J) Multiplex PCR analysis to detect *TCRB* gene rearrangements in the H254SeVT-3 genome. Tubes A and B contain Vβ-(D)Jβ assemblies; Tube C contains D-Jβ assemblies.
(K) Multiplex PCR analysis for detection of *TCRA* gene rearrangements (V-Jα assemblies).
See Figures S1, S2, and S3 for additional data.

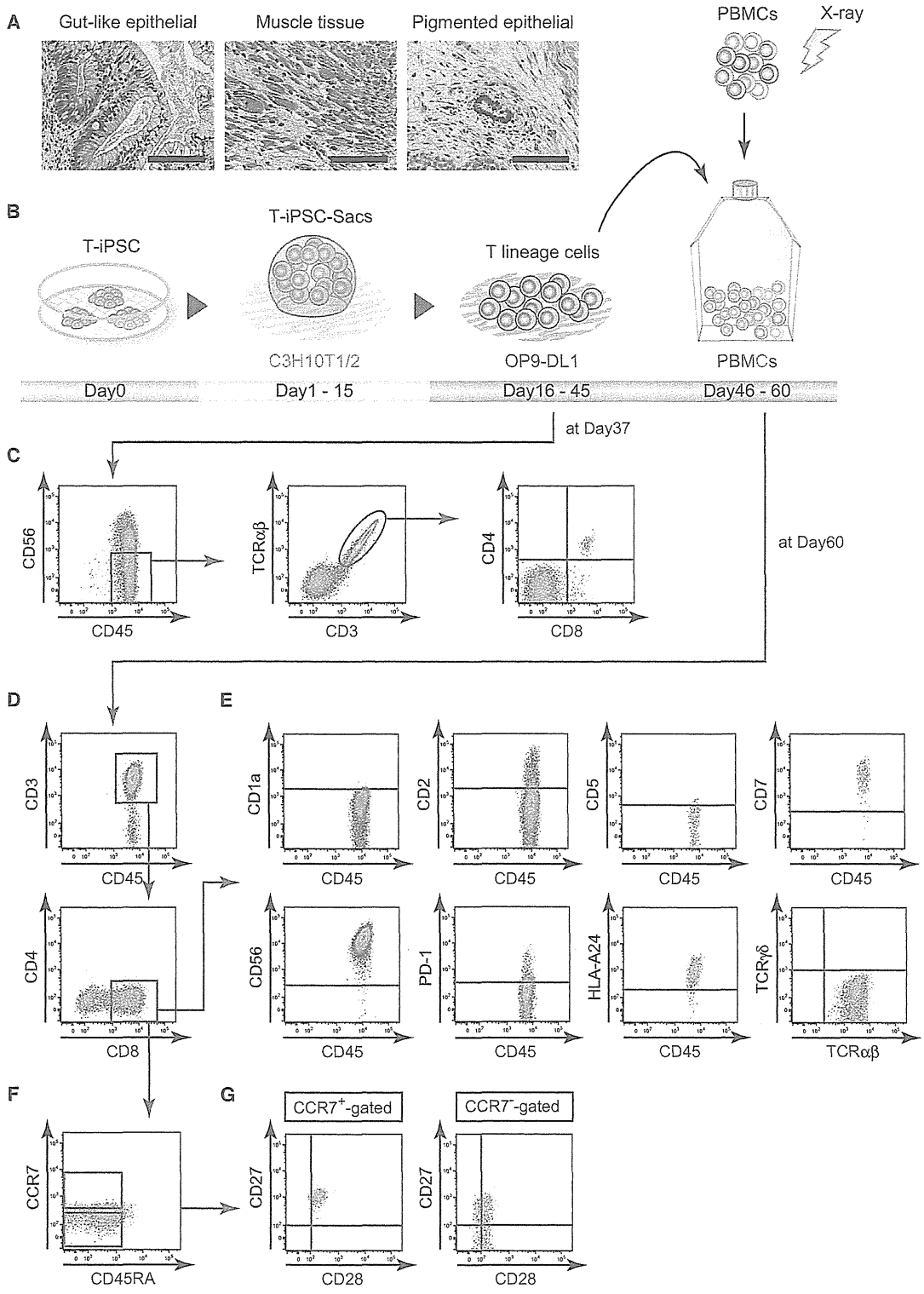

Figure 2. Redifferentiation of T-iPSCs into T Cells

(A) Representative hematoxylin- and eosin-stained sections of a teratoma formed in a NOD/ShiJic-*scid* mouse testis. H254SeVT-3 differentiated into cell lineages derived from endoderm (goblet cells in gut-like epithelial), mesoderm (smooth myocytes in muscle tissue), and ectoderm (retina cells in pigmented epithelial). The scale bar represents 100 μm.

(legend continued on next page)

the T-iPSCs at both the DN and DP stages. By contrast, some *TCRA* mRNAs at the DN and DP stages were identical to those in the T lineage cells, but others differed, and differing sequences were observed more frequently at the DP stage than the DN stage (Table S2). *RAG1* and *RAG2* expression were observed at both the DN and the DP stages, though stronger expression was observed at the DP stage (Figure S5D).

To create mature CD8 SP cells from T-iPSC-derived T lineage cells without receptor revision, we focused on TCR signaling. Turka et al. (1991) reported that TCR signaling via peptide-major histocompatibility complex (MHC) complexes during positive selection ends expression of *RAG* genes and prevents further assembly of TCR genes. They also showed that mimicking TCR signaling using CD3 antibodies had the same effect. Therefore, we tried to stimulate the TCRs of redifferentiating T lineage cells before the completion of the DN-to-DP transition (Figure 2B). For this experiment, we cultured T lineage-committed cells on OP9-DL1, stimulated them with α-CD3/28 beads or PHA (we defined this as the first stimulation) and then cocultured them with irradiated HLA-A24$^-$ PMBCs in the presence of IL-7 and IL-15, which are required for the generation of memory phenotype CD8$^+$ T cells (Kaneko et al., 2009; Prlic et al., 2002; Tan et al., 2002). After 14 days, CD8 SP cells appeared (Figure 2D). These were deemed to be derivatives of H254SeV-3 based on their expression of HLA-A24 (Figure 2E). These CD8 SP cells did not express the immature thymocyte marker CD1a, but they were positive for CD56, which is expressed on CD8$^+$ T cells cultured in vitro (Lu and Negrin, 1994). In addition, these cells expressed CD7 and some CD2, but not CD5. On the one hand, they did not express PD-1, a marker of exhausted T cells (Figure 2E). On the other hand, some of them expressed the memory T cell markers CCR7, CD27, and CD28 simultaneously, thus representing a central memory T cell phenotype (Figures 2F and 2G) (Romero et al., 2007).

To test whether the redifferentiated CD8 SP cells would recognize the same epitope on the same HLA, the entire population of redifferentiated T cells was mixed with the A24/Nef-138-8(WT) tetramer and subjected to flow-cytometric analysis (Kawana-Tachikawa et al., 2002). Most of the CD8 SP cells were stained positively by the A24/Nef-138-8(WT) tetramer, but not by the control tetramer, which represents HIV-1 envelope-derived peptides (RYLRDQQLL; Figure 3A and data not shown). We then collected the A24/Nef-138-8(WT) tetramer-reactive CD8$^+$ cells and expanded them once again using α-CD3/28 beads or PHA stimulation (defined as the second stimulation; Figure 3A). Finally, after several independent redifferentiation experiments, we obtained A24/Nef-138-8(WT) tetramer-reactive CD8 SP cells (reT-1, reT-2.1, reT-2.2, and reT-3). As expected, sequence analysis of *TCRA* and *TCRB* mRNAs in the redifferentiated CD8 SP cells revealed that the TCR gene rearrangement pattern was identical to that in the H25-#4 original T cell clone (Figure 3B and Table 1).

To determine whether the redifferentiated CD8 SP cells were of the T cell lineage, we used quantitative PCR to compare gene-expression profiles among redifferentiated CD8 SP cells, PB CD4$^+$ and CD8$^+$ T cells, and the H25-#4 original T cell clone. As shown in Figure 3C, the expression patterns of CD3, CD4, and CD8 were similar among PB CD8$^+$ T cells, redifferentiated CD8 SP cells, and the H25-#4 original T cell clone. However, the pattern differed from those in PB CD4$^+$ T cells (Figure 3C). Cytotoxic "signature" genes such as granzyme B (*GZMB*), perforin (*PRF1*), interferon-γ (IFN-γ; *IFNG*), and FAS ligand (*FASLG*) were expressed in PB CD8$^+$ T cells. These genes were also expressed relatively strongly in redifferentiated CD8 SP cells and in the H25-#4 original T cell clone; that is, in already-primed T cells (Figure 3D). The expression patterns of several factors involved in transcription or signal transduction and of cell-surface molecules were similar among PB CD8$^+$ T cells, redifferentiated CD8 SP cells, and the H25-#4 original T cell clone (Figure 3E). To exclude the possibility that the redifferentiated CD8 SP cells had acquired natural killer (NK)-like properties during their coculture with OP9-DL1 or PBMCs, we used a complementary DNA (cDNA) microarray to analyze global gene-expression profiles in redifferentiated CD8 cells, the H25-#4 original T cell clone, and PB NK cells. Correlation and cluster analyses of the gene-expression profile of the redifferentiated CD8 SP cells showed it to be similar to that of the H25-#4 original T cell clone but different from that of NK cells (Figures 3F and 3G). These data strongly suggest that T-iPSCs are able to redifferentiate into CD8$^+$ T cells that exhibit the same antigen specificity as that of the original T cell.

Generation of Highly Proliferative T Cells through T-iPSCs

Fewer than 10^5 T lineage cells were obtained from ~3 × 10^5 T-iPSCs after coculture with C3H10T1/2 and OP9-DL1 cells. However, they could be expanded to >10^8 cells with the first stimulation (data not shown). After separating A24/Nef-138-8(WT) tetramer-reactive CD8$^+$ cells, we assessed the expansion rate induced by the second stimulation and also assessed the establishment of reT-1, reT-2.2, and reT-3. We found that these cells expanded from 100-fold to 1,000-fold within 2 weeks in the presence of IL-7 and IL-15, whereas the H25-#4 original T cell clone expanded only about 20-fold (Figure 4A). Even after 100-to-1,000-fold expansions, some cells still expressed central memory T cell markers such as CCR7, CD27, and CD28 (Figure S6). Perhaps with passage through the iPSC state, wherein telomerase activity is quite high (Marion et al., 2009; Takahashi et al., 2007), re-elongation of shortened telomeres in the H25-#4 original T cell clone gives the redifferentiated T cells high replicative potential (Monteiro et al., 1996; Weng et al., 1998). In fact, the redifferentiated T cells carried longer telomeres than the original T cell clone (Figure 4B), an overall process that we call

(B) Schematic illustration of redifferentiation from T-iPSCs into T cells.
(C) Flow-cytometric analysis of the phenotypes of differentiating T lineage cells at 37 days after starting redifferentiation.
(D and E) Flow-cytometric analysis of the phenotypes of T cells at 60 days after starting redifferentiation. Fluorescence-activated cell sorting (FACS) analyses revealed CD8 single-positive maturation (D) and expression of several T cell markers (E).
(F and G) Memory phenotypes of redifferentiated CD8$^+$ T cells. There existed memory-phenotyped cells such as all positive for CCR7 (F), CD27, and CD28 (G). Data are representative of at least three independent experiments. See Figures S3, S4, and S5 and Table S2 for additional data.